

Slamming and green water loads on a ship sailing in regular waves predicted by a coupled CFD–FEA approach

Jialong Jiao^{1,2}, Songxing Huang¹, Tahsin Tezdogan³, Momchil Terziev³, C. Guedes Soares^{2*}

¹School of Civil Engineering and Transportation, South China University of Technology,
Guangzhou, 510641, China;

²Centre for Marine Technology and Ocean Engineering (CENTEC), Instituto Superior
Técnico, Universidade de Lisboa, 1049-001, Lisbon, Portugal;

³Department of Naval Architecture, Ocean and Marine Engineering, University of Strathclyde,
Glasgow, UK.

*Corresponding author email: c.guedes.soares@centec.tecnico.ulisboa.pt (C. Guedes Soares)

Abstract: A numerical simulation method is presented by integrating Computational Fluid Dynamics (CFD) and Finite Element Analysis (FEA) solvers to predict ship wave loads and slamming loads taking into account hydroelastic effects. The interest of this study mainly lies in the slamming and green water pressures acting on a flexible ship investigated by the coupled CFD–FEA method. Firstly, verification and sensitivity analysis of the wave loads and slamming pressures on the S175 containership evaluated by the coupled CFD–FEA method is conducted by comparing the results using different mesh sizes and time step schemes. Discussion on the effect of hydroelasticity on impact pressures is also conducted. Then a comprehensive analysis on the global motions, wave loads, slamming and green water pressures of the ship in different regular wave conditions is undertaken. Finally, a simplified bow flare and bottom slamming pressure estimation method based on the seakeeping data of incident wave and ship global motions are proposed, which can reduce the computational burden of the two-way fluid-structure interaction simulations when impact pressure is concerned.

Keywords: ship hydroelasticity; wave loads; slamming; whipping; green water on deck;
fluid-structure interactions

1. Introduction

The prediction of ship motions and wave loads has long been an important research branch in the field of naval architecture and ocean engineering. Over the past decades, theoretical and numerical methods for predicting ship seakeeping performance and wave loads have been dramatically developed, which mainly include 2D strip theory (Salvesen et al., 1970; Rajendran and Guedes Soares, 2016) and 3D panel theory (Mei et al., 2020; Li et al.,

2017). Due to the increasing dimensions of ships, hydroelastic effects should also be considered in addition to the global motions and wave loads of ships (Hirdaris et al., 2014; Jiao et al., 2019). To date, substantial work has been made on both 2D and 3D hydroelasticity theories within the framework of potential flow theory following the pioneering work of Bishop and Price (1979).

However, a critical drawback of the conventional linear hydroelasticity theories, when using 2D or 3D potential flow theory within a modal superposition framework and a beam or 3D structural finite element analysis (FEA) representation, is that they are not capable of capturing the nonlinearities involved in the fluid actions as a consequence of the assumptions involved (Hirdaris et al., 2014; Lakshmynarayanan and Hirdaris, 2020). Although different levels of nonlinear theories ranging from weakly nonlinear Froude–Krylov method (Jiao et al., 2020), and a 3D transient free surface Green’s function (Datta and Guedes Soares, 2020) to a strongly nonlinear body exact method (Singh and Sen, 2007), have been developed for ship hydroelastic analysis, some complex flow phenomena such as flow separation, water splash, wave breaking and viscous effects cannot be reproduced in the framework of potential flow method.

The advent of high-performance computing technology over recent years has resulted in the development of fully nonlinear time-domain CFD methods in the prediction of ship hydrodynamics (Wang and Wan, 2020). CFD methods can implicitly consider the nonlinearities arising due to the hydrodynamic actions and aid in visualizing flow features. Although tremendous advances have been made in the CFD simulations of rigid ship hydrodynamics, investigations of ship wave loads and hydroelasticity by using CFD are relatively scarce. Fortunately, the FEA of the structural part can be coupled with the CFD solver for the estimation of wave loads and structural deformations of flexible ships and offshore structures (Bakica et al., 2020).

Recently, the application of the coupled CFD–FEA method for investigating the wave loads and structural responses of ships has been carried out using both one-way and two-way partitioned coupling methods. For example, Ma and Mahfuz (2012) developed a finite element tool for structural analysis of a composite multi-hull structure in a two-way coupling manner using the ANSYS Workbench platform. Lakshmynarayanan and Hirdaris (2020) and Lakshmynarayanan and Temarel (2020) developed both one-way and two-way Fluid Flexible Structure Interaction (FFSI) methods to study ship wave loads and hydroelastic responses using the commercial software of STAR-CCM+ and Abaqus. Shi et al. (2019) investigated hydroelastic water-entry impact dynamics of elastic AUVs by LS-DYNA software based on the arbitrary Lagrangian-Eulerian (ALE) algorithm. Takami et al. (2018) predicted global and local hydroelastic responses of a ship by coupling the CFD solver STAR-CCM+ and the dynamic explicit FEA solver LS-DYNA.

Ships can experience water impacts when sailing at high speed or in severe sea states, or both. According to Xu and Duan (2009), the hydrodynamic impact can be classified into four types, which have also been identified in experimental work: bow flare slamming (Hermundstad and Moan, 2005), bottom slamming (Shin et al., 2018), green water on deck (Fonseca and Guedes Soares, 2005) and wave slap (Guedes Soares et al., 2007). Slamming is a strongly nonlinear response, which can result in critical structural failure and onboard

facilities damage. The prediction of slamming loads is a very challenging subject due to the strongly nonlinear free surface and physical surface conditions during the impact ([Wang and Guedes Soares, 2017](#)). Up to now, water entry issues of both 2D and 3D structure impact with calm water have been well addressed by using different numerical and experimental approaches ([Zhao and Faltinsen, 1993](#); [Wu et al., 2004](#); [Luo et al., 2012](#); [Sun et al., 2020](#)). Ship slamming loads are usually predicted along with global seakeeping or hydroelastic analysis since the slamming event is caused by the large vertical movement of a free-running ship relative to waves. For example, [Kim et al. \(2015\)](#) estimated hull sectional impact loads by a 2D generalized Wagner model (GWM), which is strongly coupled with 3D hydroelastic governing equations of the hull in the time domain. [Rajendran et al. \(2016\)](#) calculated the hull sectional slamming force by von Karman model and coupled it with 2D hydroelastic motion equations of the hull in the time domain. Measurements of slamming pressures especially on the bow area have also been widely conducted in ship seakeeping and wave loads experiments ([Jiao et al., 2016](#); [Camilleri et al., 2018](#); [Lin et al., 2020](#); [Wang et al. 2020](#)).

Since the flow field during slamming of a ship is highly nonlinear and cannot be accurately reproduced using potential flow methods, CFD has been widely used to calculate the slamming loads and impact pressure on ships. For example, [Wang and Guedes Soares \(2016a\)](#) calculated the slamming pressure on the stern of a chemical tanker by using an ALE algorithm implemented in LS-DYNA based on the ship–wave relative motion data obtained by 2D strip theory. [Xie et al. \(2020\)](#) provided a hybrid two-step solution by combining linear seakeeping theory and the CFD method to predict asymmetrical slamming loads of a ship in oblique waves. [Jiao and Huang \(2020\)](#) and [Huang et al. \(2021b\)](#) calculated the global motion responses and bow flare slamming pressure of the S175 ship operating in multi-directional waves by a RANS method. [Lin et al. \(2021\)](#) calculated the asymmetric motion and slamming pressure of a containership due to parametric rolling in head regular waves by CFD and also compared the results with those by potential flow theory and tank model tests.

Severe slamming events can result in not only enormous local impact pressure but also hull girder global whipping responses, which are critical for the extreme wave loads and ultimate strength evaluation. Recently, the CFD–FEA coupling method has already been used to study ship wave loads and whipping responses even though the relevant work is very scarce. For example, [McVicar et al. \(2018\)](#) studied slam-induced bending moments of wave-piercing catamarans in head seas by both one-way and two-way interaction methods. [Takami et al. \(2018\)](#) predicted the slamming pressure and whipping loads on a containership in regular waves and also compared them with potential flow theory and tank model test data. [Takami and Iijima \(2020\)](#) developed a two-way coupling method in both a weakly coupled manner and a strongly coupled manner. The developed two-way coupled methods were validated via a comparative study against the available experimental results and the straightforward one-way coupled CFD and FEA in terms of the rigid body motion, bending moment, and local water pressure.

A two-way FFSI method by coupling CFD and FEA solvers for the prediction of ship hydrodynamics, wave loads, and slamming loads have been reported in the authors' recent work ([Jiao et al., 2021a](#); [Jiao et al., 2021b](#)), where the numerical method is applied to the S175 containership. Verification and validation of the ship motions and wave loads predicted

by the coupled CFD–FEA method have also been conducted in [Jiao et al. \(2021a\)](#) and [Huang et al. \(2021a\)](#). However, the slamming and green water pressures on the S175 ship model are not much studied or reported, even though they are extensively concerned in the research field and very important for ship design and operation. Therefore, this study mainly focuses on the investigation of the nonlinear impact loads including slamming and green water pressures of the S175 containership based on the CFD–FEA co-simulation.

This paper is organized in the following way. A brief description of the coupled CFD–FEA method is reported in Section 2 and more details of the method can be found in [Jiao et al. \(2021a\)](#) and [Jiao et al. \(2021b\)](#). Verification and sensitivity study on the prediction of ship motions, wave loads and impact pressures is undertaken in Section 3. For the sake of completeness, some representative results of global motions and wave loads of ships in different wavelength and wave height conditions are reported in Section 4. A comprehensive study of the slamming and green water pressures on the ship in different conditions are reported in Section 5. Moreover, in Section 6 a simplified slamming pressure estimation method based on the seakeeping data of incident waves and ship global motions is proposed to predict the bow flare and bottom slamming pressure, which can reduce the computational burden of the two-way FFSI simulations when impact pressure is concerned. The main conclusions obtained from this study are summarized in Section 7.

2. Numerical method and model setup

In this study, a two-way coupled CFD–FEA simulation method with the commercial software STAR-CCM+ and Abaqus based on the SIMULIA co-simulation engine is presented. The co-simulation is conducted with a standard S175 containership for illustration. The details of the co-simulation method and numerical model setup are described in this section.

2.1 The S175 containership model

In this paper, the numerical calculations are applied to a standard S175 type containership model with a scale ratio of 1:40. Only the bare hull is involved for the seakeeping and wave loads investigations, i.e., the rudder, propeller and bilge keels are not appended to the body. The main dimensions of the model- and full-scale ship are listed in Table 1. The body plan of the hull in full scale is illustrated in Fig. 1. The longitudinal distribution of mass and vertical bending stiffness of the ship in full scale is shown in Fig. 2. It is noted that the vertical bending stiffness of the hull is assumed to be constant longitudinally and the value was determined to meet the two-node natural frequency of vertical bending vibration of the hull.

Table 1 Main particular of the S175 ship and model

Item	Full-scale	Model
Scale	1:1	1:40
Length between perpendiculars (L)	175 m	4.375 m
Breadth (B)	25.4 m	0.635 m

Depth (D)	19.5 m	0.488 m
Draft (T)	9.5 m	0.238 m
Displacement (Δ)	23,711 t	370 kg
Block coefficient (C_B)	0.562	0.562
Midship section coefficient (C_M)	0.990	0.990
Prismatic coefficient (C_P)	0.568	0.568
Longitudinal centre of gravity (LCG) from Aft Perpendicular (AP)	84.980 m	2.125 m
Vertical centre of gravity (VCG) from Base Line (BL)	8.5 m	0.213 m

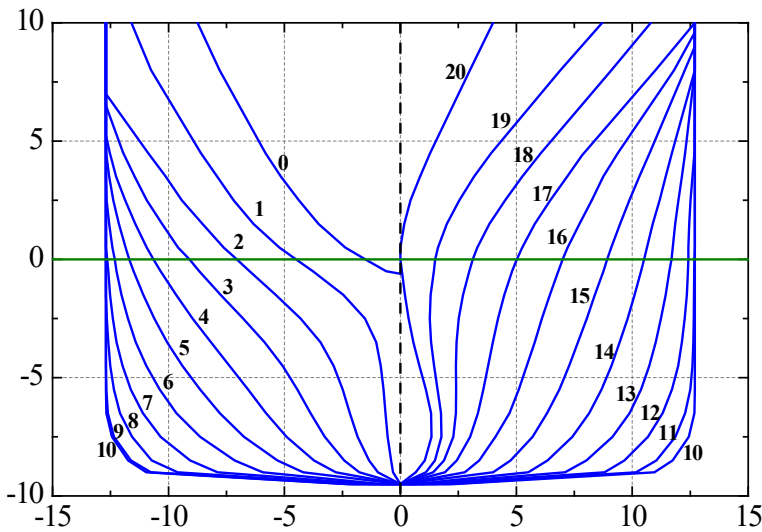


Fig. 1 Body plan of the S175 ship hull in full-scale (in meter)

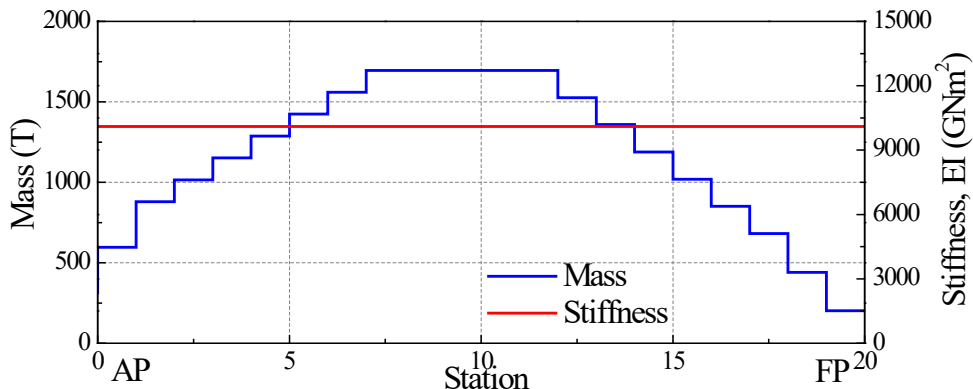


Fig. 2 Longitudinal distribution of mass and vertical bending stiffness in full scale

For the investigation of the impact pressures on the ship when sailing in severe waves, an array of 12 pressure sensors are arranged on the bow flare and bow bottom areas for slamming pressure measurement. Moreover, an array of 11 pressure sensors are arranged on the front deck area for green water pressure measurement. The exact locations of these pressure sensors are depicted in Fig. 3. For the sake of symmetry, the pressure monitoring points are arranged on the port side or middle longitudinal plane of the hull.

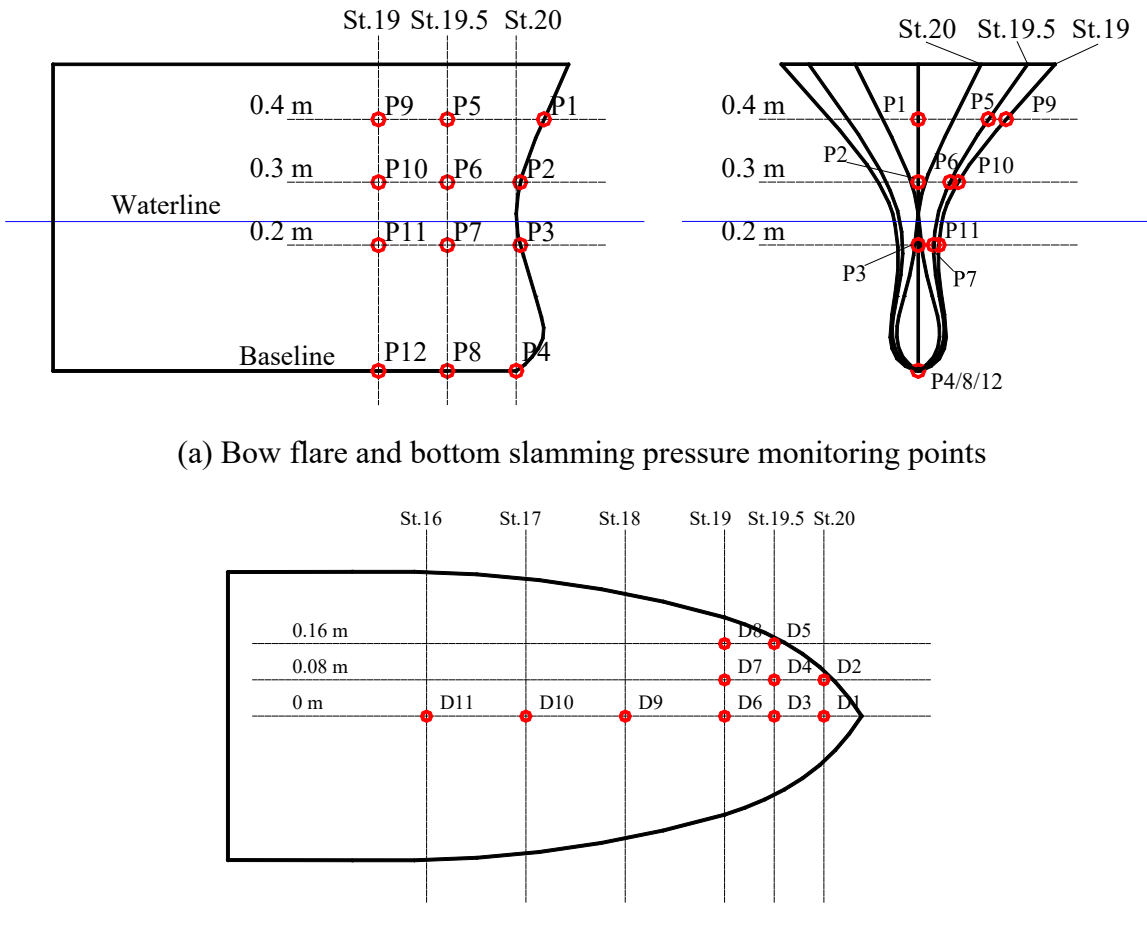


Fig. 3 Arrangement of the slamming and green water pressure sensors

2.2 Hydrodynamic model

The finite volume method (FVM)-based commercial software STAR-CCM+ is applied for the fluid flow solution. The unsteady, viscous, turbulent and incompressible flow around the ship hull is governed by the continuity and Navier–Stokes equations. A second-order upwind scheme is used to discretize the convection term. A predictor-corrector approach is used to link the continuity and momentum equations. The Semi-Implicit Method for Pressure Linked Equations (SIMPLE) is employed to achieve an implicit coupling between pressure and velocity. The Realizable k - ϵ turbulence model is adopted to solve the continuity equation and momentum equation. The Volume of Fluid (VOF) method is used to simulate the free surface between the water and the air by solving an additional transport equation for an extra scalar variable known as the volume fraction. A High-Resolution Interface Capturing (HRIC) discretization scheme is used to track sharp interfaces between the two immiscible fluid components.

A general view of the computational domain is displayed in Fig. 4. The extent of the computational domain is $-2L < x < 2.5L$, $0 < y < 1.5L$, and $-2.3L < z < 1.1L$ for all the computational cases (where L is the ship length between perpendiculars). The origin of the coordinate system coincides with the aft perpendicular of the ship at the free surface of calm water. The

dimensions of the computational domain in which the discretized equations are solved are determined by referring to the standards of the ITTC recommendations (ITTC, 2011). Within the background region of the computational domain, an overset region is defined around the ship to model the rigid body motions. The transmission of fluid flow data between the overset region and background region at each time step is realized based on the overset technique.

The fifth-order Stokes waves are used in this study. For accurate simulation of the incident waves, the Euler Overlay Method (EOM) is applied to the solution by replacing the source term in the conservation equations (Takami et al., 2018; Zhang et al., 2021; Nisham et al., 2021). The EOM forcing wave boundary condition is applied on the side boundary, outlet, and inlet to maintain the elevation and velocity of the wave by forcing agreement with the theoretical results (Jiao et al., 2021c). This will also prevent the reflection of waves from the boundary walls instead of establishing wave damping. By using the EOM method, a relatively smaller fluid domain can be used compared with the traditional wave damping approach, e.g. used in Tezdogan et al. (2016), which can largely reduce the computation burden of co-simulation. As seen in Fig. 4, for the inlet, outlet, side and bottom boundaries, the boundary condition of velocity inlet is specified; for the top boundary, the boundary condition of pressure outlet is specified. A longitudinal symmetry plane is used to halve the computational domain, to reduce the computational cost. A no-slip boundary condition is applied on the hull surface.

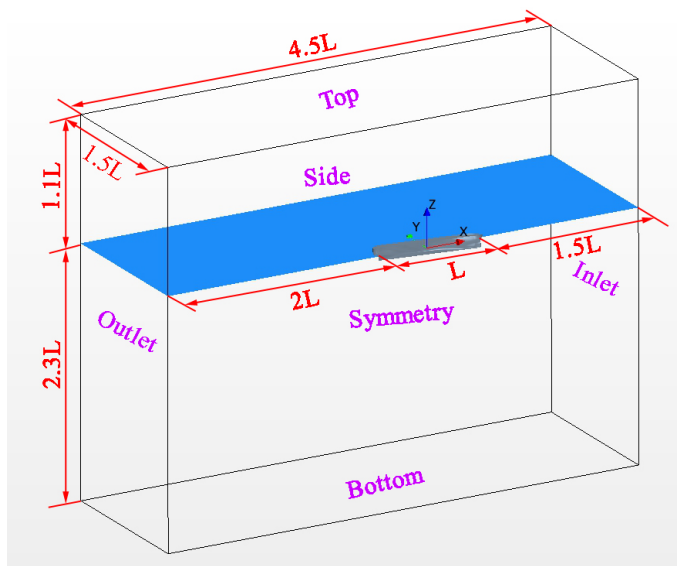


Fig. 4 An overview of the numerical wave tank

A trimmed Cartesian grid technique is used for discretizing the 3D fluid domain. Accordingly, the ensuing mesh is made up effectively of unstructured hexahedral cells with trimmed cells adjacent to the ship model. The trimmed cells are identified as hexahedral cells. Local refinement of the grid is performed near the hull and the free surface. A very slow expansion rate is used to maintain mesh connectivity. An overall view of the mesh in the computational domain around the hull body is seen in Fig. 5, which includes 4.33 million cells in total among which 1.4 million cells are located in the overset region.

The prism layer mesher generates orthogonal prismatic cells near the boundaries and is used especially for walls with no-slip conditions. This helps to simulate the near-wall flow accurately and resolve the boundary layers and separated flow near the walls with the no-slip boundary condition. The thickness of the prism layer and the number of cells are determined according to the wall y^+ desired in the flow simulation. A boundary layer mesh of 8 cells near the hull is selected (y^+ value lies in 30–60). The distribution of the y^+ value on the hull for Case 5 shown in Table 2 is displayed in Fig. 6.

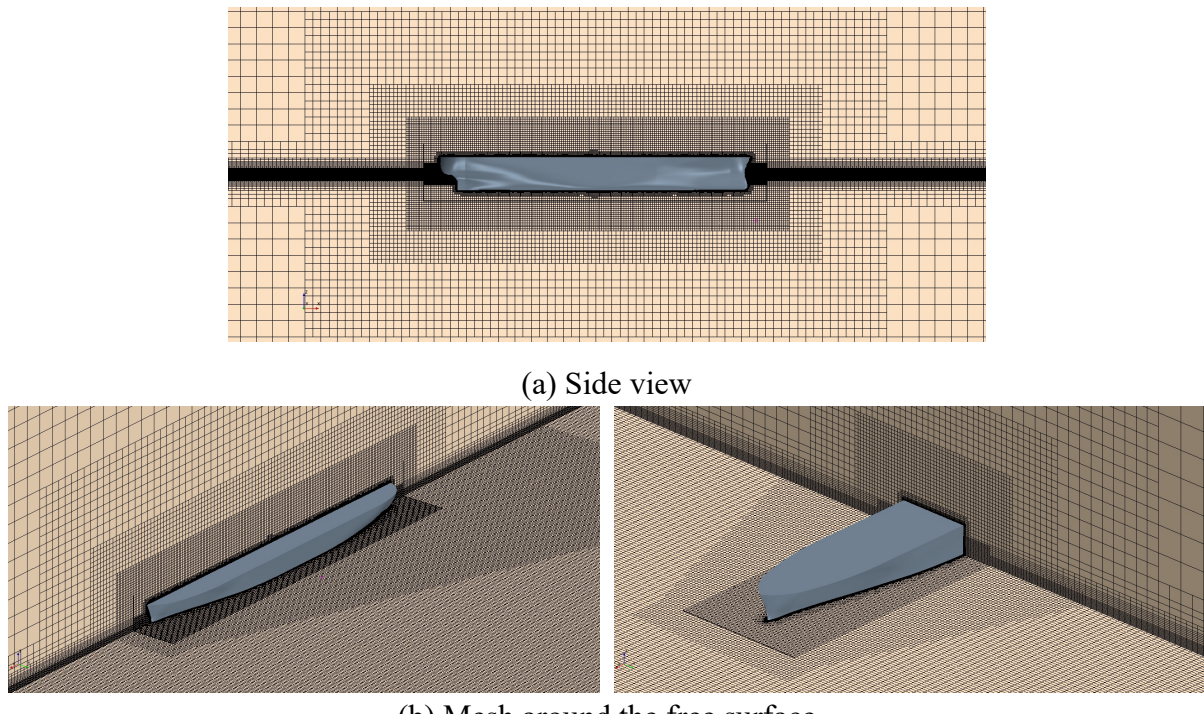


Fig. 5 General view of the mesh around the hull

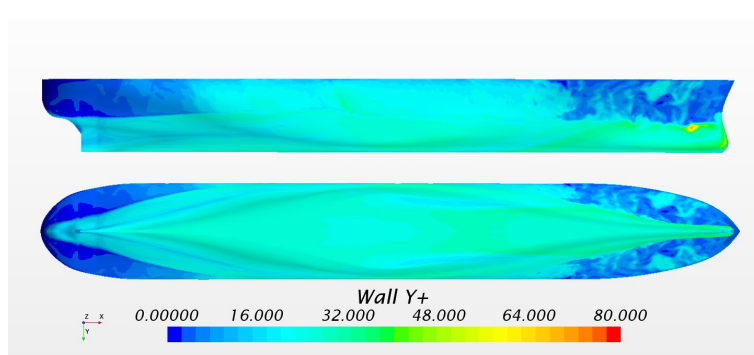


Fig. 6 Wall y^+ distribution on the hull

2.3 Structural model

The finite element method (FEM)-based commercial software Abaqus is applied for the structural response solution. A dynamic-implicit method that uses an extension of the Newmark- β scheme is adopted as the time integration scheme. A direct step-by-step

integration is used where the governing equations are integrated over the discretized time steps.

The added mass due to hull motion and vibration is explicitly accounted for in the CFD solver in the two-way coupling method. Thus, a structural finite element (FE) model in vacuum is built for the structural response analysis. A FE model that comprises a backbone beam and surface shell is created to present the hull structure of the S175 ship. This is very similar to the segmented model used in hydroelasticity experiments. The surface shell includes 21 segments that are linked to the nodes of the corresponding beam elements rigidly using kinematic coupling constraints (see Fig. 7). The backbone beam, which has 20 beam elements and 21 nodes, is modelled using 1D uniform beam elements (B31). The backbone beam has a rectangular hollow cross-section with a dimension of 60 mm×60 mm×4 mm for external width by external height by wall thickness, respectively. The material property of the beam is defined as that of steel. The backbone beam is positioned at the height of the vertical centre of gravity of the model. The hull surface is modelled using unstructured shell elements (SFM3D3) consisting of 10,357 elements and 5,348 nodes which are rigidly connected to the beam nodes. Through the kinematic coupling constraint, the motion and deformation of the hull surface are fully determined by the corresponding beam nodes, while the elastic deformation of the hull surface due to external fluid pressure is suppressed. This makes the shell of the FE model hull to be different from the real ship hull plate.

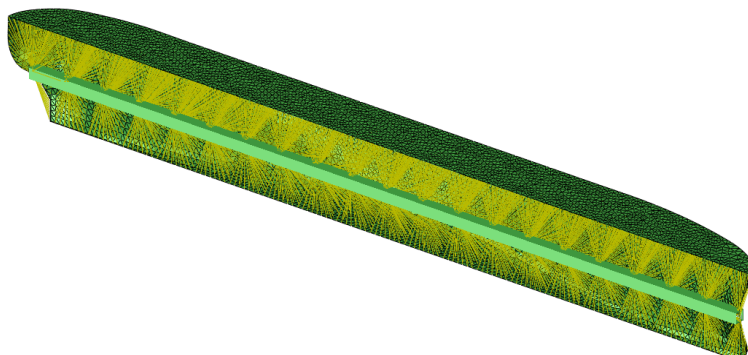


Fig. 7 The FE elements of the hull and the constraints

Fig. 8 shows a general arrangement of the structural model viewed from the side and top directions. A total of 20 cuts are provided from Sections #1 to #20, where the sectional loads such as vertical bending moment (VBM) and vertical shearing force (VSF) are measured. It is noted that the body plan curves in Fig. 1 correspond to the cross-sections at Stations 0 to 20 (vertical dashed lines in Fig. 8). Concentrated mass points (carmine square) are distributed at the centre of the beam element (green line) between adjacent nodes (blue circles) according to the mass distribution data in Fig. 2, while the shell surface elements are massless. The crosses (orange lines) denote connections between the surface shell of each segment and the relevant beam node.

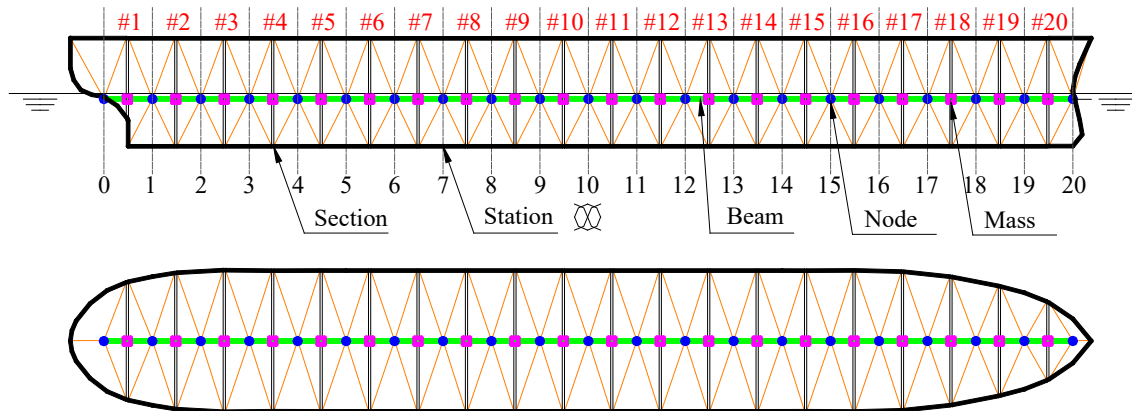


Fig. 8 Sketch of the structural model hull

2.4 Fluid-structure interactions approach

For the time-independent (steady-state) FSI problems, only the final converged solution is desired. In this case, an explicit coupling, where the exchange of information takes place once per time step, is preferred to calculate the steady-state solution (Lakshmynarayanan and Hirdaris, 2020). On the other hand, for the transient FSI problem, the results change as time evolves, where usually the outcome for the new time step is dependent on the previous time steps. In this case, the behaviour of the system over time is typically of interest and an implicit coupling scheme is preferred. In this study, a two-way coupling method is used to solve the strong coupling FSI problems of ship hydroelasticity in an implicit coupling scheme. A partitioned algorithm is adopted to execute the two-way coupling, where separate solvers for fluid and structure are employed so that information is exchanged at the interface sequentially and solved iteratively.

Fig. 9 demonstrates the calculation procedure of parallel algorithm during implicit coupling simulation, where both CFD and FEA codes do the calculation simultaneously. Several iterations between the CFD and FEA solvers will take place during each coupling time step, Δt . The number of such iterations per time step is critical for the stability and accuracy of the coupled simulations. At every iteration step, the fluid pressure and wall shear stress calculated by the fluid solver are exported into the structural solver as an external load; the structure solver feeds back the node displacement data of the structure to the fluid solver to update the structure surface, where both the overset mesh and morpher techniques are used in STAR-CCM+.

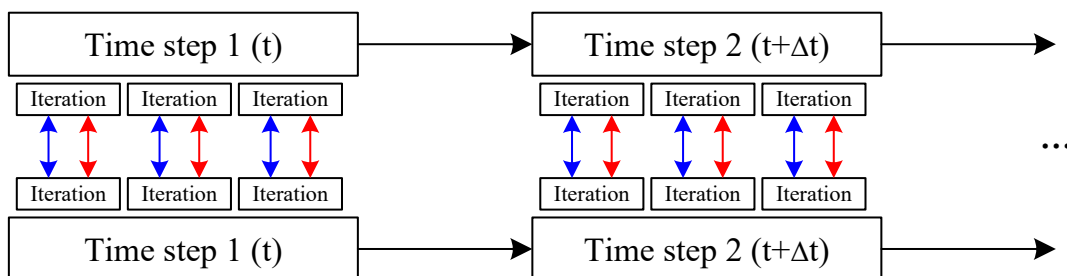


Fig. 9 Framework of the implicit coupling procedure

2.5 Simulation cases

The CFD–FEA numerical simulations for the ship sailing in regular head waves are performed according to the cases listed in Table 2. In the table, $\omega_{2\text{-node}}$ denotes the wet 2-node natural frequency of the model hull. This study mainly focuses on investigating large amplitude ship motions and slamming loads in moderate and harsh wave conditions. A speed of $Fn=0.275$ which is the preferred value in ITTC benchmark studies is used for all the cases. In Cases 1 to 5, the wavelength to ship length ratios in the range of 0.8–1.2 is used to obtain large vertical ship responses at or near the ship–wave matching frequency, where a basic wave height of $H=120$ mm (full-scale 4.8 m) is used. In Cases 5 to 7, different wave heights in the range of $H=120\text{--}240$ mm (full-scale 4.8–9.6 m) are used to calculate ship slamming and whipping responses for different wave severities in the resonant frequency case of $\lambda/L=1.2$. The numerical simulations are performed by work stations with a single node Intel(R) Core i-9 CPU with 18 cores, clock speed of 3.0 GHz and 64 GB of physical memory. All simulations are run at least 10 s for attaining stable results of ship motion responses in regular waves. The run time for cases with different mesh densities and time steps are mentioned in Section 3. For the selected mesh size and time step used for general simulations in this study, it takes about 24 h to compute the ship model response per physical 1 s.

Table 2 Numerical simulation conditions

Case ID	Speed (Fn)	Wave height (H , mm)	Wave length (λ/L)	Wave frequency (ω , rad/s)	Encounter frequency (ω_e , rad/s)	Wave steepness (H/λ)	Note
1	0.275	120	0.8	4.193	7.424	0.0343	$\omega_{2\text{-node}}=7.491\omega_e$
2	0.275	120	0.9	3.954	6.825	0.0305	$\omega_{2\text{-node}}=8.149\omega_e$
3	0.275	120	1.0	3.751	6.335	0.0274	$\omega_{2\text{-node}}=8.779\omega_e$
4	0.275	120	1.1	3.576	5.926	0.0249	$\omega_{2\text{-node}}=9.385\omega_e$
5	0.275	120	1.2	3.424	5.578	0.0229	$\omega_{2\text{-node}}=9.971\omega_e$
6	0.275	180	1.2	3.424	5.578	0.0343	$\omega_{2\text{-node}}=9.971\omega_e$
7	0.275	240	1.2	3.424	5.578	0.0457	$\omega_{2\text{-node}}=9.971\omega_e$

3. Verification of the FSI method

Numerical simulations can contain certain errors that cause the results to differ from the actual values. Thus, it is essential to evaluate the precision of the numerical results by conducting verification and validation analyses (Terziev et al., 2020). A systematical uncertainty and verification study on the sensitivity of grid density, time step and fluid domain size on the motions, acceleration, VBM and VSF predicted by the present coupled CFD–FEA method has been undertaken in the authors' previous work (Huang et al., 2021a), where the uncertainty analysis on slamming pressure and green water pressure is however not included. Therefore, this study mainly focuses on the uncertainty analysis of slamming pressure and

green water pressure. Discussion on the effect of hydroelasticity on impact pressures is also conducted. Moreover, in the authors' previous work (Jiao et al., 2021b; Huang et al., 2021a), the present CFD–FEA coupling method has been well validated by comparing with the existing experimental and theoretical data of the S175 ship in the literature (Chen et al., 2001; Watanabe et al., 1989; Fonseca and Guedes Soares, 2004; Lakshmynarayanan and Temarel, 2020).

3.1 Verification procedure

It is known that the uncertainties caused by the modelling and simulation of fluid dynamics by the CFD solver are generally much larger than the uncertainties associated with the structural responses by the FEA solver. Therefore, the present uncertainty study only involves ship response by changing a set of CFD control strategies such as mesh size and time step while the FEA scheme is not changed. The numerical simulation error and uncertainty mainly includes contributions from iteration number, grid size and time step. It is known that the uncertainty in the iteration step is negligible compared with the grid size and time step (Wilson et al., 2006). Therefore, only grid uncertainty (U_G) and time step uncertainty (U_T) are involved in the present verification study. Case 5 ($\lambda/L=1.2$, $H=120$ mm), where ship–wave resonant response occurs, is used for the uncertainty analyses.

The verification procedure proposed in the ITTC (2017) is used through convergence studies. The grid and time step convergence studies are performed using three solutions which are refined systematically with a reasonable refinement ratio $r_i=\sqrt{2}$. $S_{i,1}$, $S_{i,2}$ and $S_{i,3}$ are defined to be the solutions with the fine, medium and coarse input parameter, respectively (for grid uncertainty analysis i is replaced by G and when for time step uncertainty analysis i is replaced by T). Changes between medium-fine $\varepsilon_{i,21}=S_{i,2}-S_{i,1}$ and coarse-medium $\varepsilon_{i,32}=S_{i,3}-S_{i,2}$ solutions are used to define the convergence ratio:

$$R_i = \varepsilon_{i,21} / \varepsilon_{i,32} \quad (1)$$

Four modes of convergence can occur: (i) when $0 < R_i < 1$, monotonic convergence (MC); (ii) when $-1 < R_i < 0$, oscillatory convergence (OC); (iii) when $R_i > 1$, monotonic divergence (MD) and (iv) when $R_i < -1$, oscillatory divergence (OD). For conditions (iii) and (iv), the numerical uncertainty cannot be estimated. Generally, the preferred state is (i) monotonic convergence, in which case the numerical error $\delta_{REi,1}^*$ and order of accuracy p_i can be estimated via the generalized Richardson Extrapolation (RE) approach:

$$\delta_{REi,1}^* = \frac{\varepsilon_{i,21}}{r_i^{p_i} - 1} \quad (2)$$

$$p_i = \frac{\ln(\varepsilon_{i,21} / \varepsilon_{i,32})}{\ln(r_i)} \quad (3)$$

The factor of safety approach is then used to define the uncertainty U_i where an error estimate from RE is multiplied by a factor of safety $F_S=1.25$ to bound simulation error:

$$U_i = F_S |\delta_{REi,1}^*| \quad (4)$$

For condition (ii), the numerical uncertainty can be estimated simply by bounding the error within oscillation of maximum S_U and minimum S_L using the following equation:

$$U_i = \frac{1}{2}(S_U - S_L) \quad (5)$$

3.2 Grid sensitivity

To evaluate the grid sensitivity and uncertainty, numerical simulations are carried out with three suites of grids, i.e. fine, medium and coarse. The minimum grid size of the fine mesh, medium mesh and coarse mesh are 0.005 m, 0.007 m and 0.010 m, respectively. A comparative view of the three grid schemes is shown in Fig. 10. It is noted that different mesh density is only applied to the overset region, while the mesh density in the background region remains unchanged for all three schemes to ensure high-quality incident waves can be generated throughout the whole computational domain. An enlarged view around the overset region is additionally presented in each figure for a better comparison and visualization. For the fine mesh scheme, the overset mesh is much smaller than the background mesh. For the medium mesh scheme, the overset mesh has the same size as the background mesh. For the coarse mesh scheme, the overset mesh is much larger than the background mesh. The total number of cells in the fluid domain and the solving time, which corresponds to the time for simulating the ship model response of approximately 10 s physically, for each set of the grid schemes are given in Table 3.

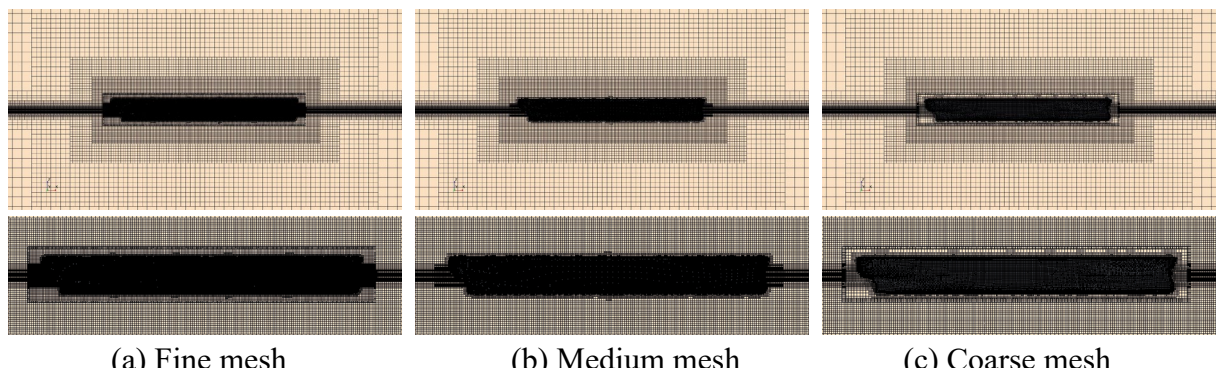


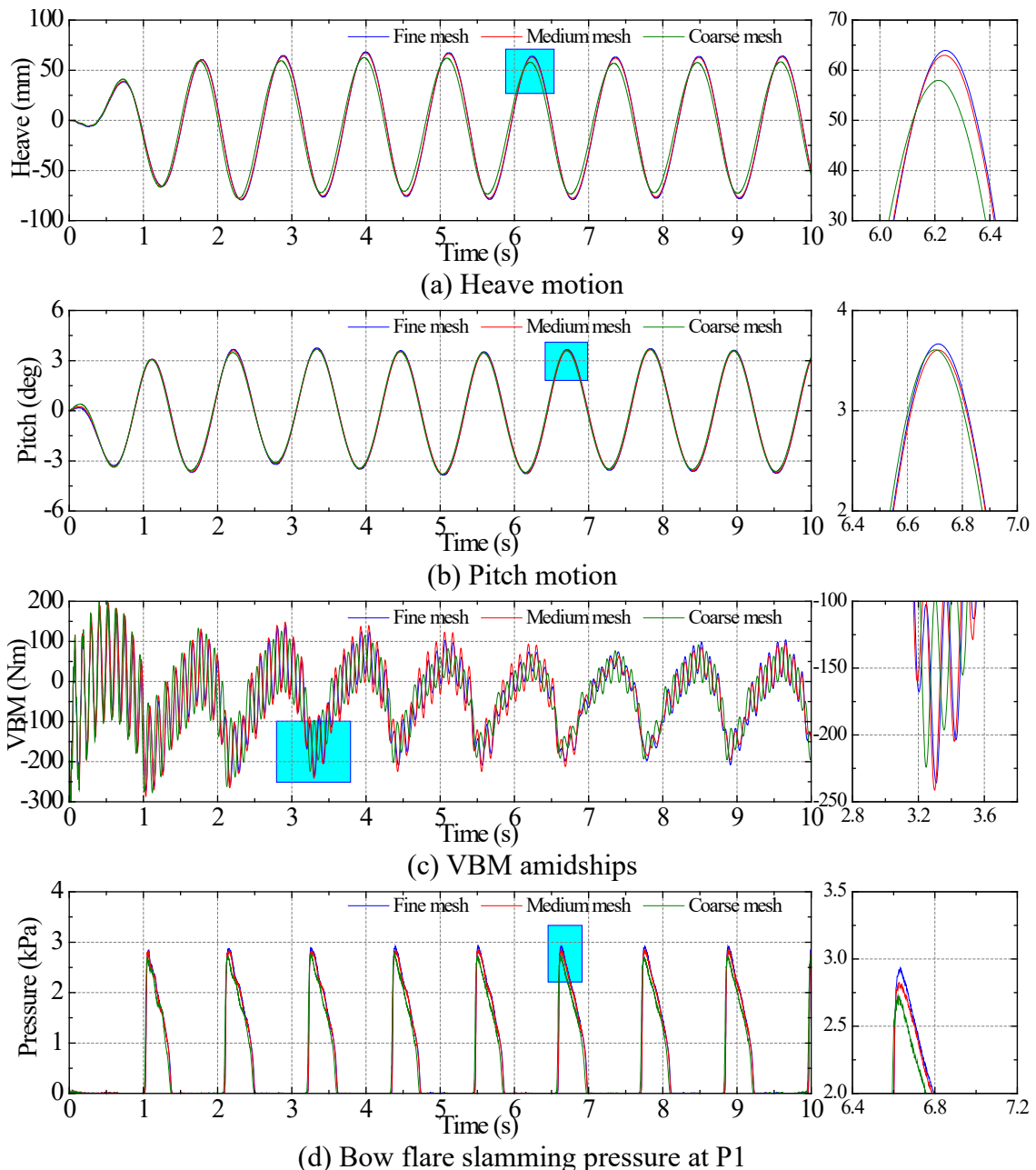
Fig. 10 Comparative view of the three mesh schemes

Table 3 Grid parameters of each mesh scheme

Grid	Time step (s)	Minimum grid size (m)	Cell number (million)	Solving Time (h)
Fine	0.001	0.005	5.62	332
Medium	0.001	0.007	4.33	213
Coarse	0.001	0.010	3.73	161

The time series of the heave, pitch, VBM amidships and impact pressure (including bow flare slamming pressure at P1, bow bottom slamming pressure at P4 and green water pressure at D3) obtained with the three grids are compared in Fig. 11. It is worth mentioning that original signals of global motions and loads are presented while the impact pressures were

low-pass filtered with a cut-off frequency of 450 Hz to remove noises. The time-series results indicate that the heave, VBM and impact pressure at P1 and D3 by the coarse mesh reveals obvious deviation from the remaining grids, while the curve representing the medium mesh shows good agreement with the fine mesh. However, the difference between curves by different grid schemes is smaller for the pitch motion and bow bottom pressure at P8. The verification parameters of motions and loads for the grid size convergence study are demonstrated in Table 4. As it is seen, monotonic convergence and reasonably small levels of uncertainty are obtained for heave and impact pressures. Although monotonic divergence is obtained for pitch, the difference between different schemes is small and the pitch result is sufficiently reliable. Oscillatory convergence is obtained for VBM and it is clear that the difference of VBM among the three schemes is larger than any other kind of signal.



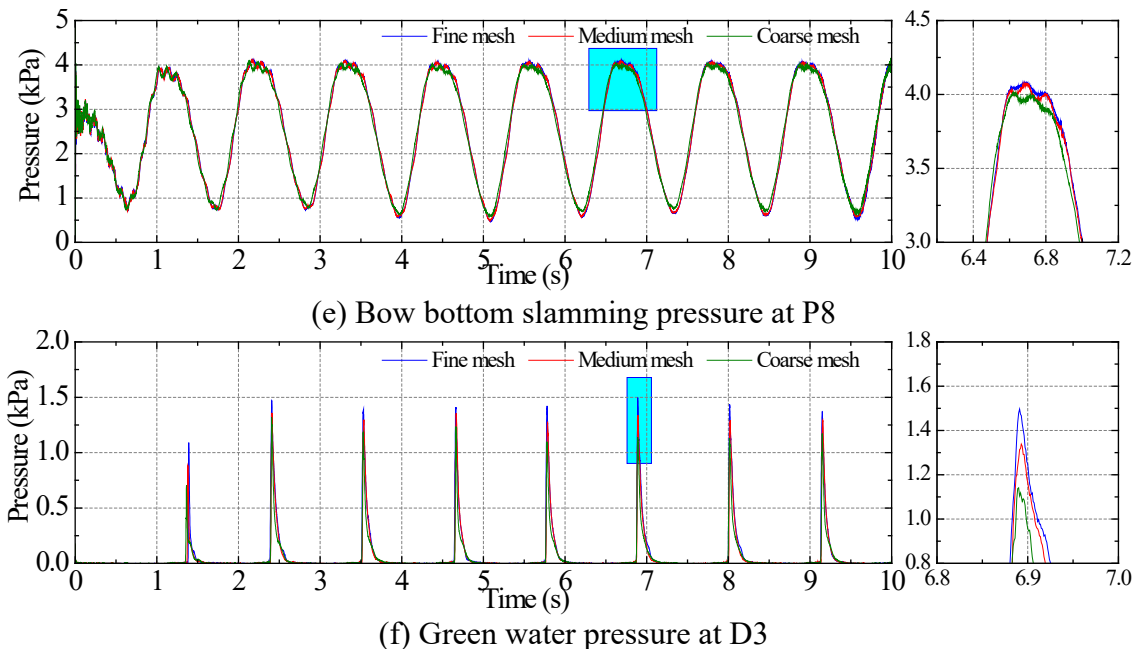


Fig. 11 Comparison of time series of motions and loads by different grid schemes

Table 4 Convergence study for motions and loads by different grid schemes

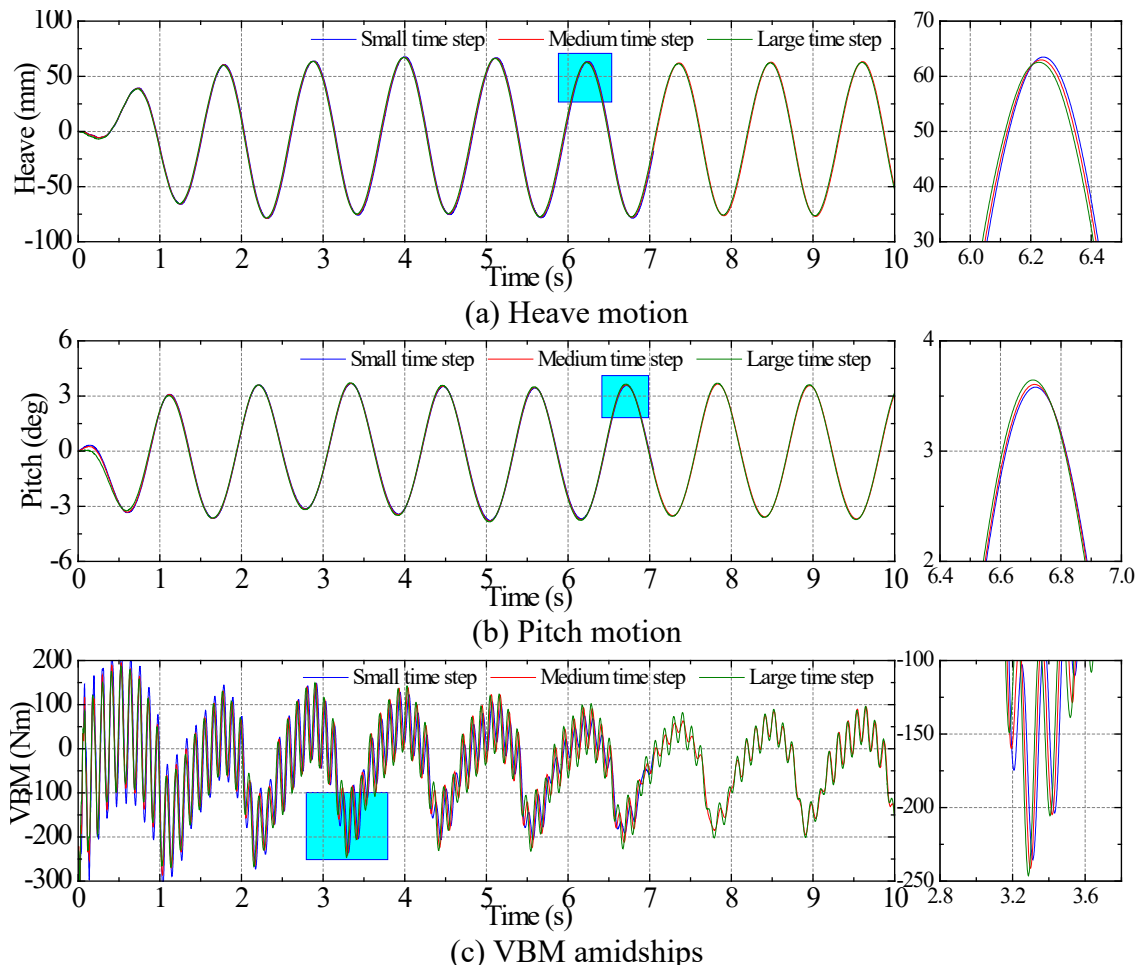
Parameter		Amplitude value			Pressure peak (kPa)		
Description	Symbol	Heave (mm)	Pitch (°)	VBM (Nm)	P1	P8	D3
Fine	S_{G1}	64.331	3.663	-235.594	2.920	4.086	1.503
Medium	S_{G2}	63.068	3.612	-241.722	2.824	4.072	1.332
Coarse	S_{G3}	58.124	3.602	-224.956	2.724	4.010	1.145
Change between Medium-fine	$\varepsilon_{G,21}$	-1.263	-0.051	-6.128	-0.096	-0.014	-0.171
Change between Coarse-medium	$\varepsilon_{G,32}$	-4.944	-0.01	16.766	-0.100	-0.062	-0.187
Convergence ratio	R_G	0.255	5.1	-0.366	0.960	0.226	0.914
Convergence type	/	MC	MD	OC	MC	MC	MC
Order of accuracy	p_G	-3.938	N/A	N/A	-0.118	-4.294	-0.258
Numerical error	$\delta_{REG,I}^*$	-0.00588	N/A	N/A	-19.917	-0.00002	-7.322
Uncertainty	U_G	0.007355	N/A	8.383	24.897	0.000029	9.153

3.3 Time step sensitivity

The verification analysis for the time step can be conducted similarly. For the simulation of ship slamming and whipping responses, the time step is recommended to be set smaller than 1/100 of the 2-node natural vibration period so that the high-frequency whipping loads and impact peaks can be well captured. The uncertainty analysis on time step is carried out using three kinds of the time step, i.e. small (0.0007 s), medium (0.0010 s) and large (0.0014 s). These three simulations are performed using the medium grid resolution with 4.33 million cells, which is the best choice as a compromise between accuracy and cost in the above

analysis.

The time series of heave, pitch, VBM amidships and impact pressure (including bow flare slamming pressure at P1, bow bottom slamming pressure at P4 and green water pressure at D3) obtained with the three time steps are compared in Fig. 12. To remove high-frequency noises the impact pressures were low-pass filtered with a cut-off frequency of 600 Hz, 450 Hz and 300 Hz for the results of small, medium and large time steps, respectively. The calculation time for the ship model response to solve approximately 10 s of physical time by using the small, medium and large time step schemes is 282 h, 213 h, and 132 h, respectively. It can be seen that the influence of the time step on the results is generally small, and the curve of the medium time step agrees well with that of the small time step. The uncertainty analysis results for the time step convergence study are listed in Table 5. Monotonic convergence and reasonably small levels of uncertainty are obtained for the majority of the signals apart from VBM.



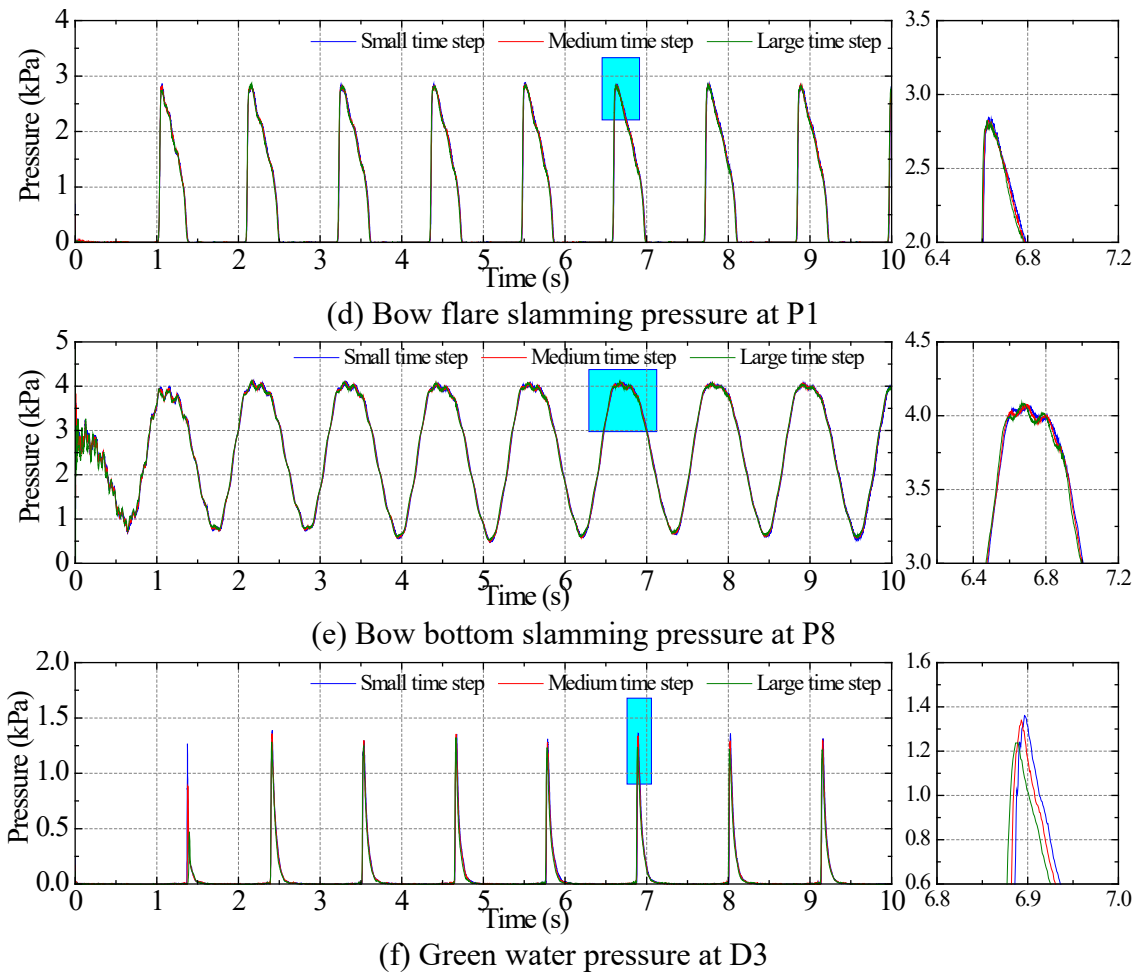


Fig. 12 Comparison of time series of motions and loads by different time step schemes

Table 5 Convergence study for motions and loads by different time step schemes

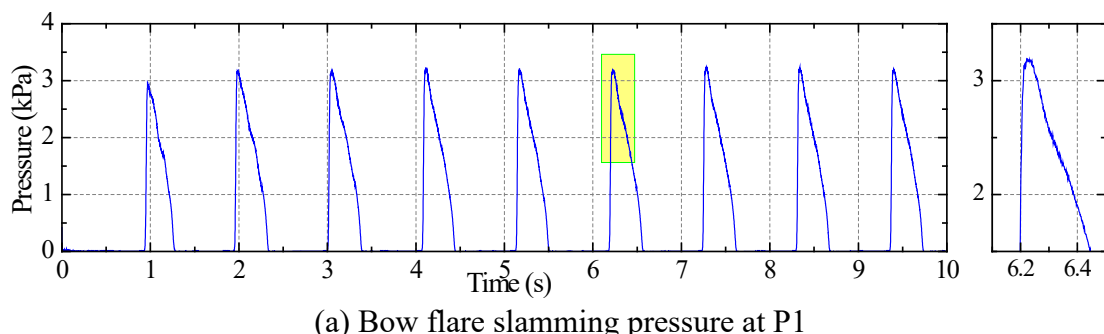
Parameter		Amplitude value			Pressure peak (kPa)		
Description	Symbol	Heave (mm)	Pitch (°)	VBM (Nm)	P1	P8	D3
Fine	S_{T1}	63.389	3.583	-236.221	2.847	4.065	1.362
Medium	S_{T2}	63.068	3.608	-240.937	2.826	4.076	1.337
Coarse	S_{T3}	62.504	3.642	-247.159	2.828	4.088	1.239
Change between Medium-fine	$\varepsilon_{T,21}$	-0.321	0.025	-4.716	-0.021	0.011	-0.025
Change between Coarse-medium	$\varepsilon_{T,32}$	-0.564	0.034	-6.222	-0.002	0.012	-0.098
Convergence ratio	R_T	0.5691	0.7353	0.7580	-10.500	0.9167	0.2551
Convergence type	/	MC	MC	MC	OD	MC	MC
Order of accuracy	P_T	-1.626	-0.8872	-0.7996	N/A	-0.2511	-6.971
Numerical error	$\delta_{RET,I}^*$	-0.2139	0.07971	-19.011	N/A	0.4981	-4.9E-10
Uncertainty	U_T	0.2674	0.09964	23.763	N/A	0.6226	6.07E-10

3.4 Effect of hydroelasticity on impact pressures

As is known, CFD simulations can also predict the slamming and green water pressures along with rigid body ship seakeeping calculation (Huang et al., 2021b; Jiao and Huang, 2020). However, the hydroelasticity may have certain effects on the impact pressures on a flexible hull, which is not much investigated in the existing work. Therefore, the influence of hull flexibility on the surface impact pressure is studied in this section.

The time series of bow flare slamming pressure at P1, bow bottom slamming pressure at P4 and green water pressure at D3 in Case 4 ($\lambda/L=1.1$, $H=120$ mm) are shown in Fig. 13. This case is used for illustration as the whipping dominates the hydroelastic response while the springing response is not pronounced; and the conclusion can be obtained without loss of generality. The corresponding frequency spectra of pressure by fast Fourier transform (FFT) are shown in Fig. 14.

As seen from the spectra of P1 and D3 where the transient impact pressure only lasts for a short time period during each slamming event, the high-order harmonic responses are very pronounced. In fact, the high-order harmonic responses are not caused by hydroelastic responses as very similar high-order harmonic responses can be also obtained from the impact pressure on a rigid ship by CFD simulation. However, it is noted that there is no energy component at the wet 2-node natural frequency 8.856 Hz (marked by the vertical red line) in the spectra of P1 and D3. This reveals that the influence of ship hydroelasticity on the transient impact pressure is ignorable even though 2-node whipping responses occur on the hull girder. On the other hand, only the first two orders of harmonic response can be clearly seen in the spectrum of P8 where the pulsating pressure lasts for a longer period during each slamming event. It is also noted that in the spectrum of P8 there exists a slight energy component at the wet 2-node natural frequency. To confirm this, the same spectrum in LOG scale is additionally shown in Fig. 14d. Furthermore, low-pass filtering with a cut-off frequency of 10 Hz and 7.5 Hz is applied on the time series of P8 to obtain the pressures with and without hydroelasticity effects, respectively; and the results are shown in Fig. 13b. It is seen that the hydroelasticity effect results in very slight high-frequency vibrations at the crest of the pressure curve when compared with the rigid body result, but the contribution is small.



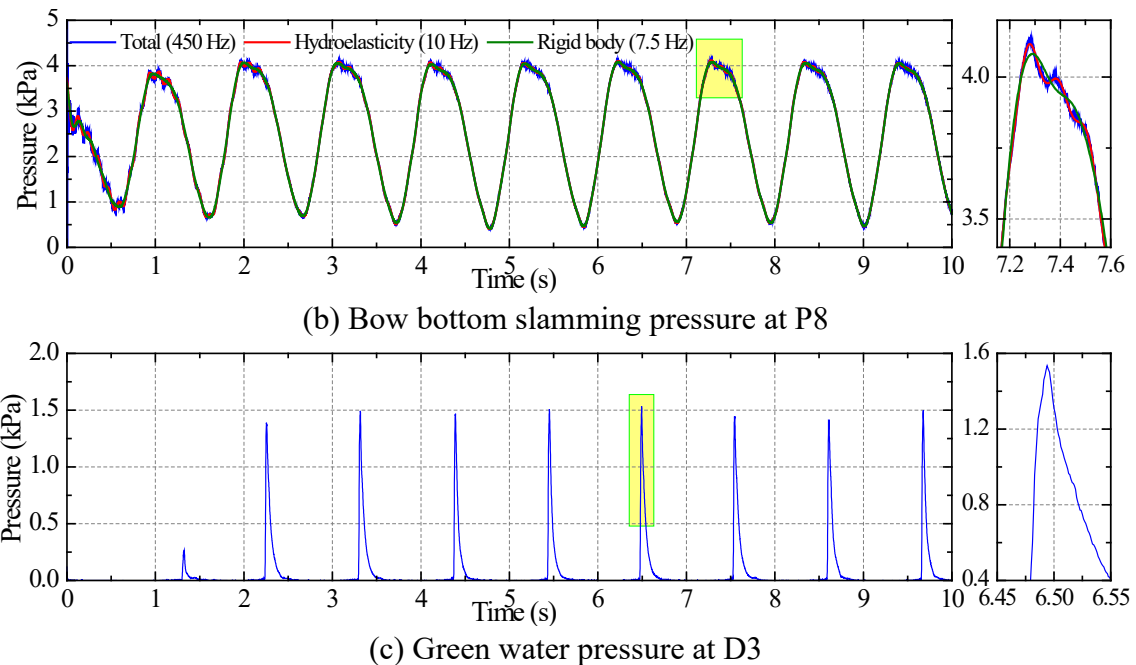


Fig. 13 Time series of slamming and green water pressures ($\lambda/L=1.1$, $H=120$ mm)

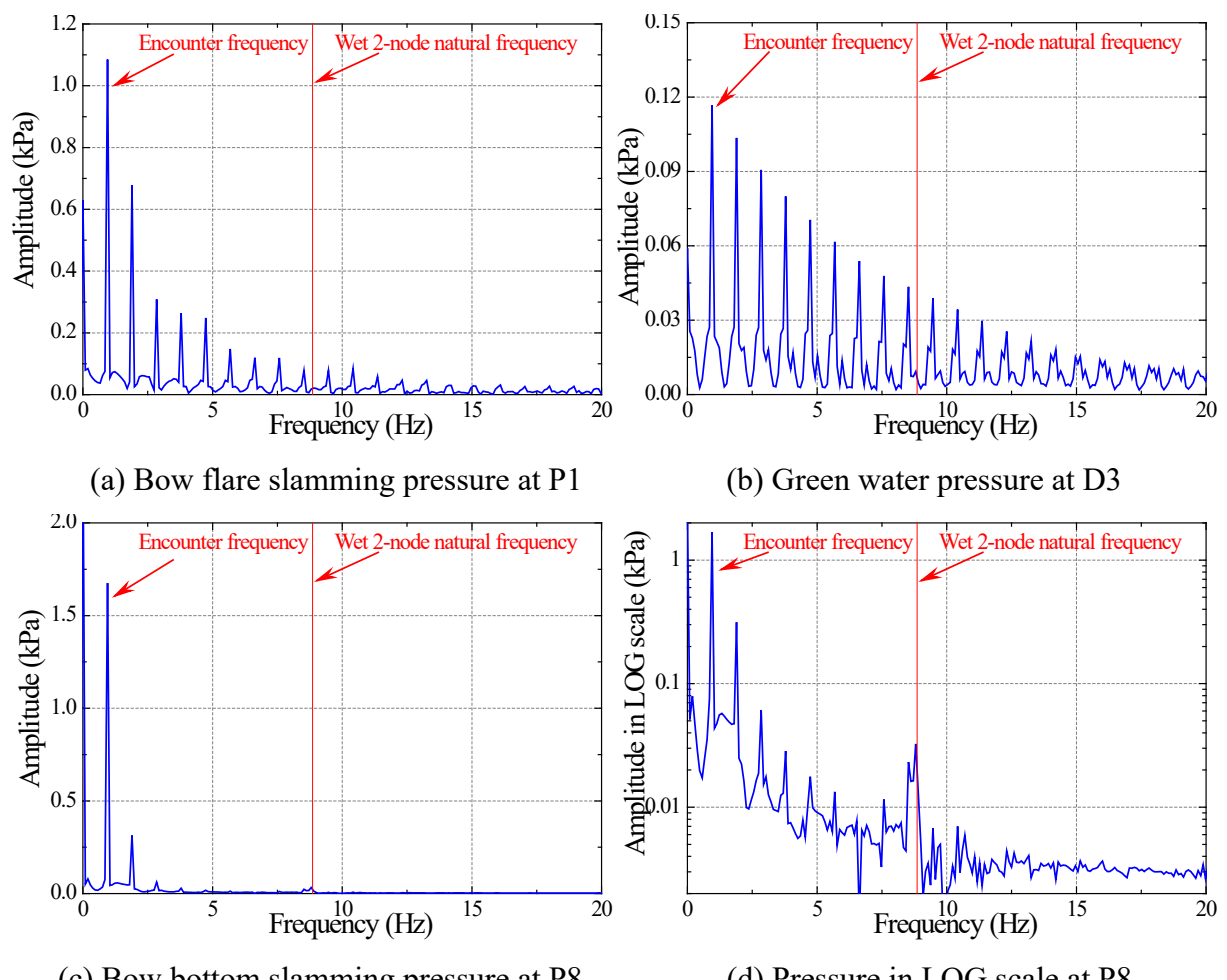


Fig. 14 Frequency spectra of the slamming and green water pressures ($\lambda/L=1.1$, $H=120$ mm)

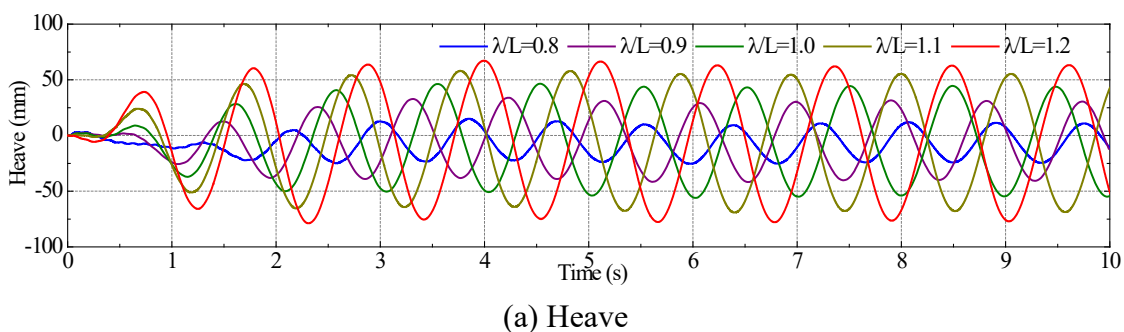
To summarize, the hull flexibility can slightly affect the pulsating pressure, which lasts for a longer period during each slamming event, by posing high-frequency vibrations at the crest of the pressure curve. However, the influence of hull flexibility on the surface impact pressure is ignorable especially for the transient impact pressure of bow flare slamming and green water on deck. The reasons are as follows. The wave-induced structural deformation of the hull girder is very small for a 175-meter-long ship prototype with normal stiffness. The deformation on larger containerships over 300 m long may be more pronounced. Moreover, the elastic deformation of the hull surface due to external fluid pressure is suppressed, while it is fully determined by hull girder vibration. The surface panels of the current FE model are different from the real hull plate. The FE model hull is however very similar to the segmented model used in hydroelasticity experiments.

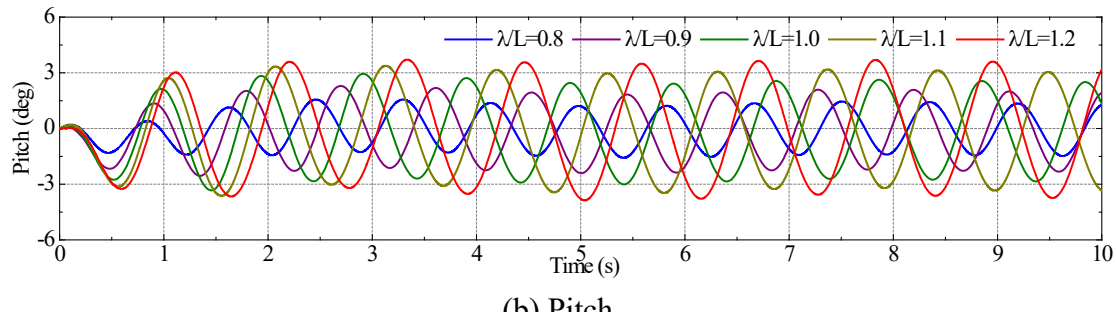
4. Global motions and wave loads

In this section, the global motions and wave loads, i.e. heave, pitch and VBM amidships, of the ship in different wave conditions are presented and analyzed, which is fundamental for the subsequent analyses of ship slamming and green water pressures associated with the global seakeeping issue.

4.1 Heave and pitch motions

The original time series of ship heave and pitch motions in different wavelength cases ($\lambda/L=0.8\text{--}1.2$, $H=120$ mm) simulated by the coupled CFD–FEA method are summarized in Fig. 15. The heave and pitch motions start from zero, which corresponds to the static equilibrium position of the ship, and they become steady approximately after three encounter waves. The crest and trough peaks of heave and pitch during the ship steady run region show certain asymmetry behaviour due to the presence of non-zero mean value caused by the sinkage or trim, respectively.





(b) Pitch

Fig. 15 The time series of heave and pitch at different wavelengths ($\lambda/L=0.8\text{--}1.2$, $H=120$ mm)

The response amplitude operators (RAOs) of heave and pitch motions with varying wavelength $\lambda/L=0.8\text{--}1.2$ are shown in Fig. 16. The heave amplitude is non-dimensionalized by z/ζ and the pitch amplitude is non-dimensionalized by $\theta/k\zeta$, where k and ζ denote wave amplitude and wavenumber, respectively. The crest and trough values of ship motion and their mean values are also presented in the figure to show the asymmetry of ship motion response. As can be seen from the results, the amplitude value of both heave and pitch increases rapidly from $\lambda/L=0.8$ to 1.2 as the encounter frequency trends to the ship–wave matching frequency. The difference between the peak values of crest and trough for heave is obvious and the trough value is much greater than the crest. This indicates that the ship was subjected to a noticeable sinkage, which is probably caused by the dynamic effects with the forward speed. The ship also experienced trim by stern motion, which results in a larger trough and smaller crest for pitch peaks.

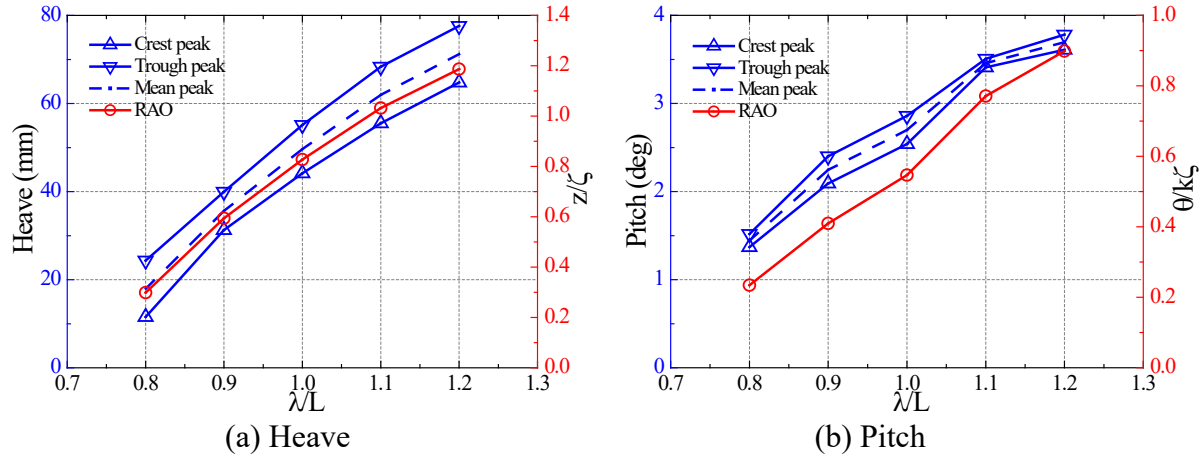


Fig. 16 Peak values distribution and RAO of motion responses ($\lambda/L=0.8\text{--}1.2$, $H=120$ mm)

The variation of the heave and pitch motions with wave height is shown in Fig. 17. The heave and pitch amplitude values increase almost linearly with the increase of wave height. However, the dimensionless results of amplitude values decrease almost linearly with the increase of wave height since the nonlinear effects such as the variation of instantaneous wetted surface become more pronounced.

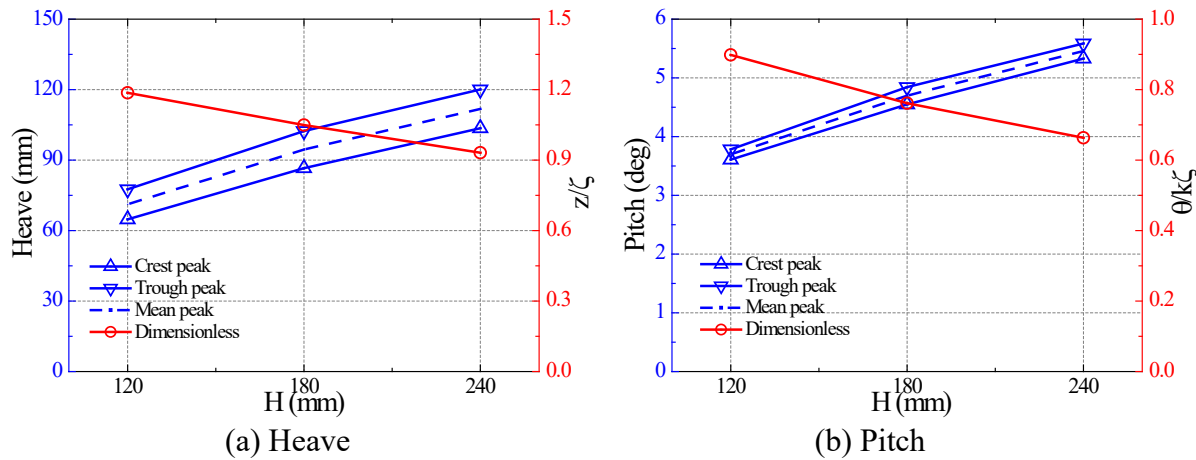
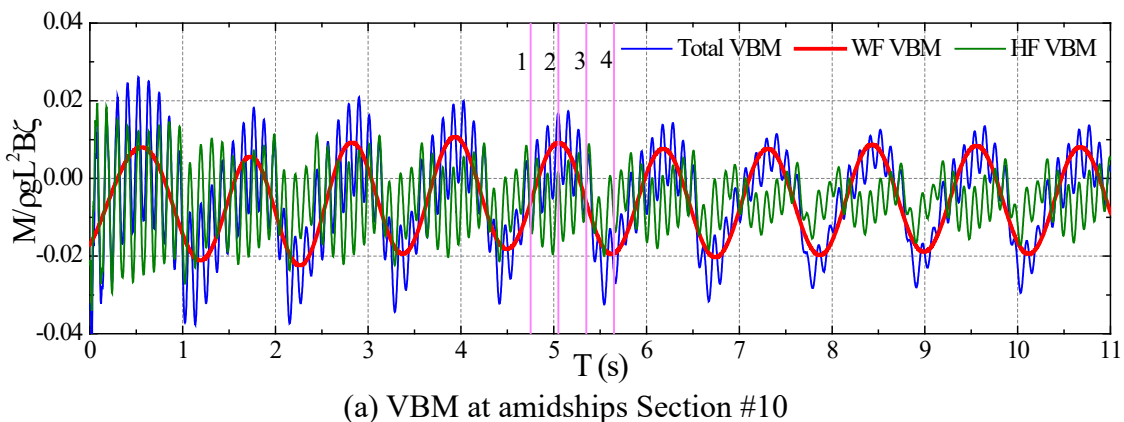


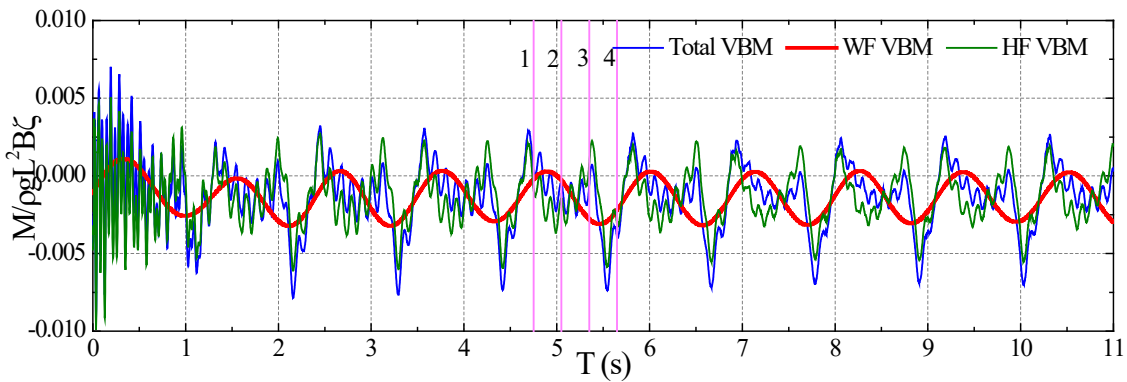
Fig. 17 Variation of motion responses with wave height ($\lambda/L=1.2$, $H=120\text{--}240$ mm)

4.2 Vertical bending moment

The time series of the wave-induced loads of VBM in one typical wave case ($\lambda/L=1.2$, $H=120$ mm) simulated by the coupled CFD–FEA method is summarized in Fig. 18, where the VBM both amidships at section #10 and the bow section #18 are presented. The VBM is non-dimensionalized by $M/\rho g L^2 B \zeta$. It is noted that the calm water VBM has been subtracted from the original VBM data to obtain the wave-induced VBM. The bandwidth pass filtering technique was also applied to divide the total VBM into two parts of wave-frequency (WF) and high-frequency (HF) components, which are also shown along with the total VBM in each graph in Fig. 18. It is seen that significant whipping loads occur in the total VBMs. The WF loads show sinusoidal behaviour in shape for both sections. The magnitude of HF whipping loads is comparatively large as the WF VBM at section #10 while it is almost threefold the WF VBM at section #18. It is also seen from the figure that the whipping loads contribute more to the total sagging VBM compared with the hogging VBM.



(a) VBM at amidships Section #10

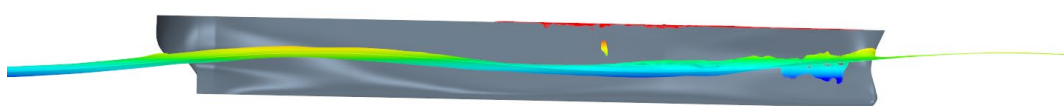


(b) VBM at bow Section #18

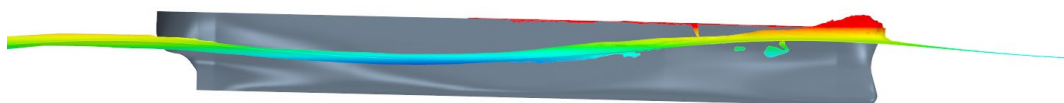
Fig. 18 Time series of VBM components in typical case ($\lambda/L=1.2$, $H=120$ mm)

Fig. 19 presents the position of the ship relative to the wave profile, which shows the slamming and green water on deck at four typical time instants corresponding to the following instants; up-crossing zero bending moment (State 1), maximum hogging occurs (State 2), down-crossing zero bending moment (State 3) and maximum sagging moment (State 4) of VBM at amidships section. The four typical time instants are also marked by the pink vertical line in Fig. 18. There exists a phase difference between the VBM signals at different longitudinal positions mainly due to the dynamic inertia force and forward speed effects. The visualization also indicates that the slamming impacts and water splash around the bow area have been well captured by the CFD solver.

The longitudinal distribution of the peak value of both total VBM and WF VBM at different sections for the typical case ($\lambda/L=1.2$, $H=120$ mm) is shown in Fig. 20. It is seen that the sagging VBM is generally much larger than the hogging VBM for both total and WF VBMs. The total sagging VBM shows strong asymmetry relative to the corresponding hogging VBM, and the largest total sagging VBM appears in front of the largest total hogging VBM due to the contribution of nonlinear whipping load components.



(a) State 1 ($t=4.75$ s)



(b) State 2 ($t=5.05$ s)

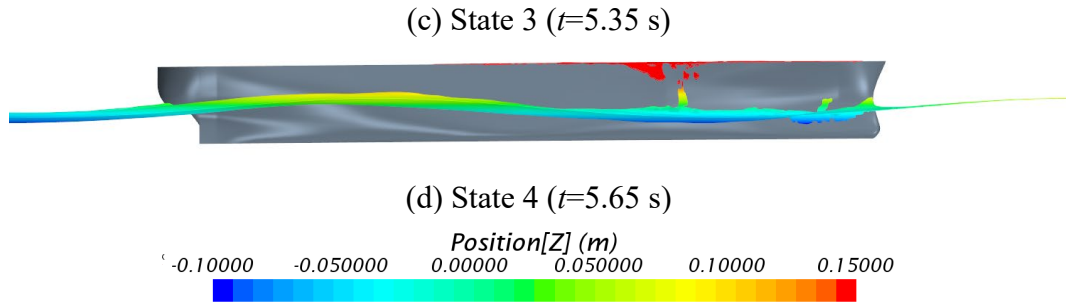


Fig. 19 Wave profile along the ship length ($\lambda/L=1.2$, $H=120$ mm)

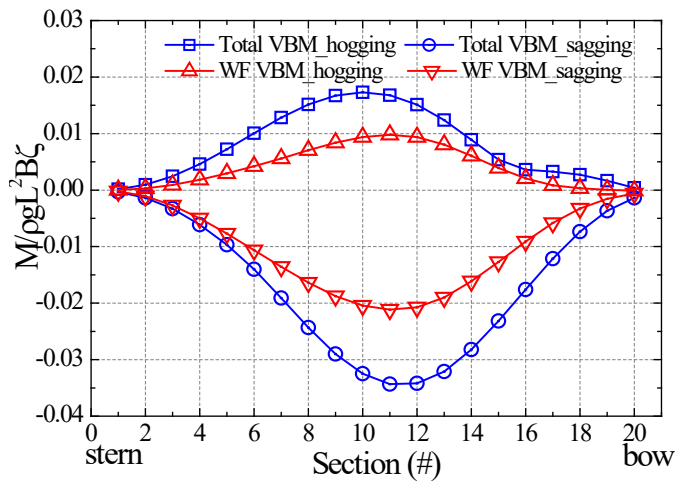
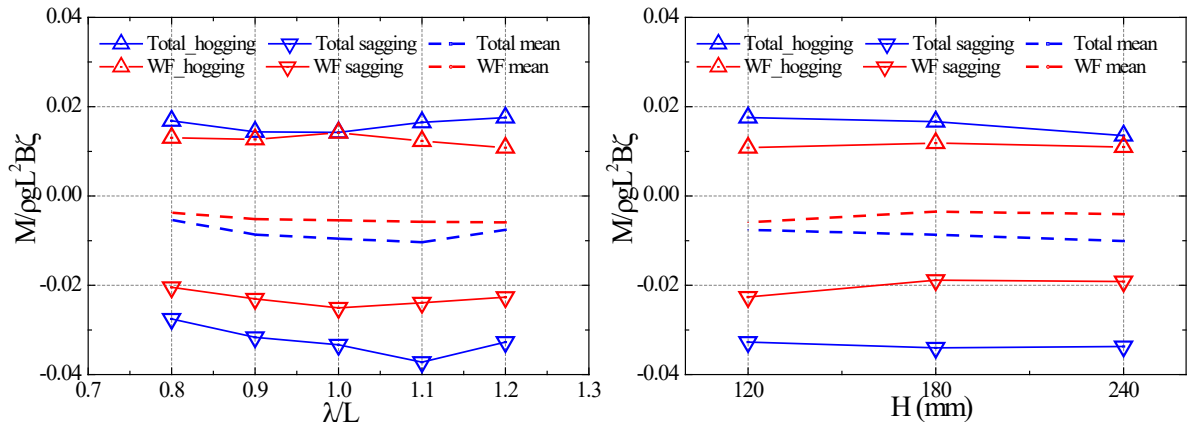


Fig. 20 Longitudinal distribution of peak value of VBM ($\lambda/L=1.2$, $H=120$ mm)

Moreover, the dimensionless VBM amidships varying with wavelength or wave height are summarized in Fig. 21. The plot provides the results for hogging and sagging VBMs and their mean value for both the total VBM and linear WF VBM. The results in Fig. 21a indicate that the largest WF VBM occurs at $\lambda/L=1.0$ while the largest total VBM occurs at $\lambda/L=1.1$ due to the higher contribution of HF slamming loads. As can be seen in Fig. 21b, the dimensionless VBM amidships especially the WF VBM is not sensitive to the varying wave height, which shows different phenomenon as the results of motion response shown in Fig. 17. The slamming-induced HF VBM contributes more to the total sagging VBM than the hogging VBM with the increase of wave height.



(a) Varying with wavelength ($H=120$ mm) (b) Varying with wave height ($\lambda/L=1.2$)

Fig. 21 Variation of the dimensionless peak value of VBM amidships in different wave conditions

5. Slamming and green water pressures

In this section, the slamming and green water pressures on the bow area of the ship in different wave conditions are systematically analyzed. The data analyses mainly focus on the time series of the impact pressures and their variation and spatial distribution characteristics.

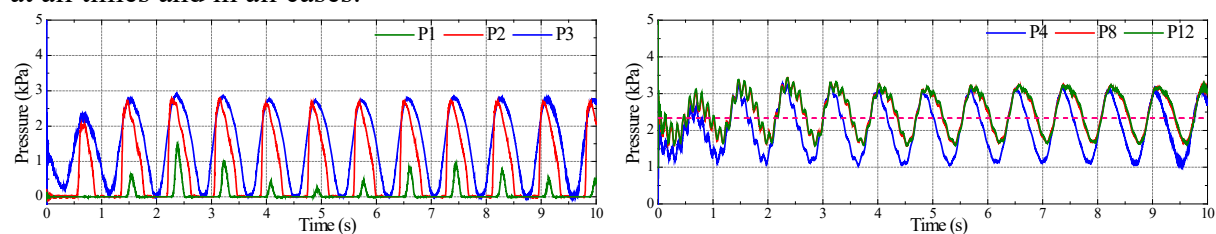
5.1 Slamming pressures on bow flare and bottom areas

5.1.1 Varying with wavelength

The time series of the slamming pressure at typical measurement points P1–3 on the bow flare area and typical measurement points P4, P8 and P12 on the bow bottom area in different wavelength conditions ($\lambda/L=0.8–1.2$, $H=120$ mm) are summarized in Fig. 22, where the results were low-pass filtered with a cut-off frequency of 450 Hz to remove the high-frequency noises. It is seen that the time series of the impact pressures evolve steadily after the initial two encounter waves, which confirms the applicability of the co-simulation method in the prediction of impact pressures. The occurrence frequency of slamming events is the same as the wave encounter frequency. Bow slamming event occurs in all five conditions due to the relatively large wave height, but the severity of slamming is different.

The pressure peak of the bow flare slamming event, which is mainly determined by the water entry velocity and deadrise angle at a specific point, is not very sharp for all these cases since the sea state is not severe enough. The pressure signal at P1 generally has the sharpest peak mainly due to its relatively low dead-rise angle compared with P2–3 in the large bow flare area. The peak at P3 is very smooth/blunt since it has a negative dead-rise angle (inclined inward angle). Only slight wave contact pressure occurs at P1 in the case of $\lambda/L=0.8$ due to the relatively low vertical motion amplitude of the ship. The peak pressure of bow flare slamming generally shows an increasing trend with longer wavelengths as the vertical motion amplitude increases.

Unlike the bow flare slamming impact signal, the bow bottom pulsating pressures fluctuate around their static equilibrium position (marked by a red dash line) that is caused by hydrostatic pressure. For a specific case, the largest peak value of bow bottom pulsating pressure at P4, P8 and P12 is comparable, although there is a slight decreasing trend from P4 to P12 due to the decrease of immersed depth during bow down motion. The point at P4 almost emerges from the water in the case of $\lambda/L=1.0–1.2$ while P8 and P12 remain immersed at all times and in all cases.



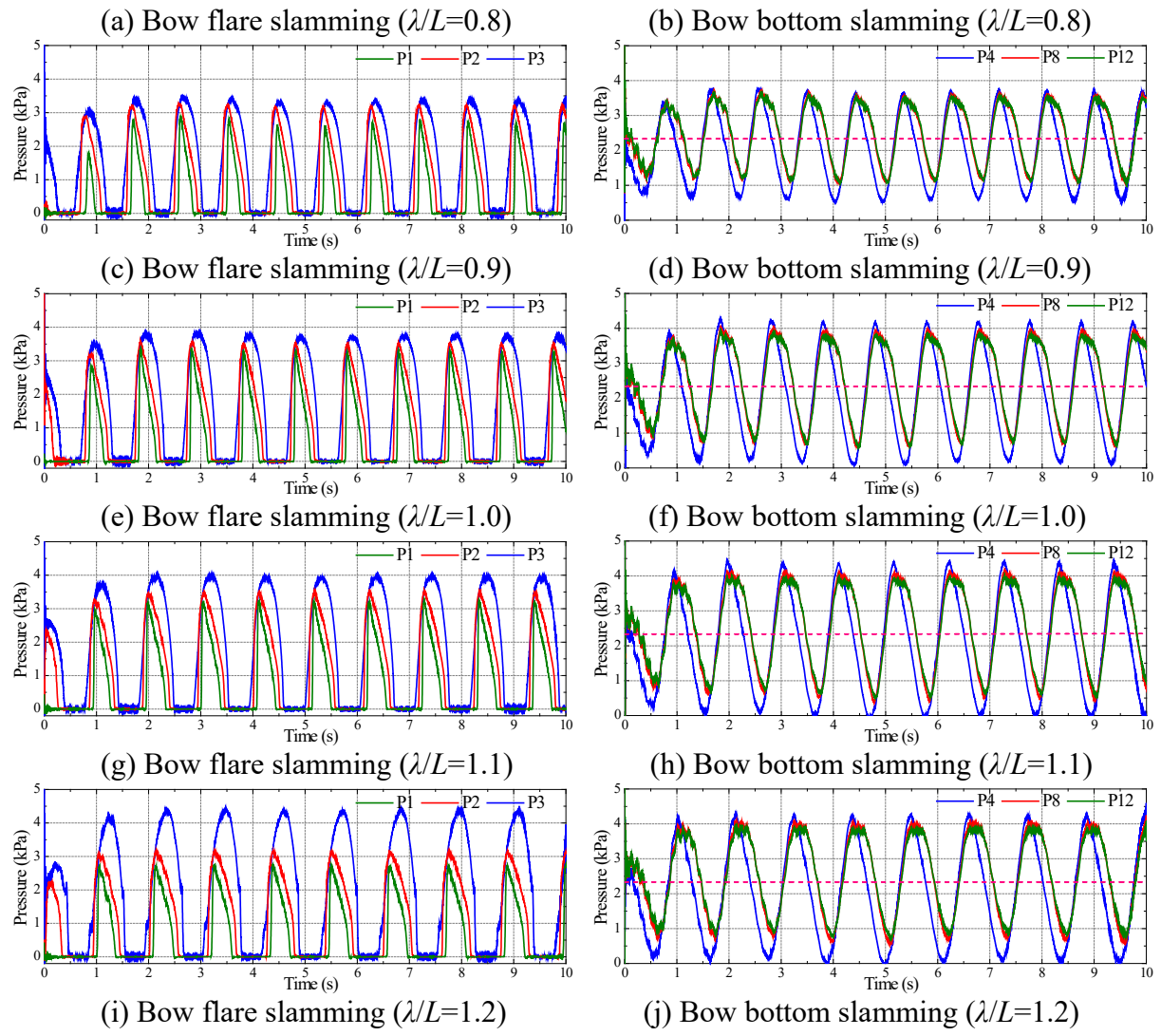


Fig. 22 Time series of typical slamming pressure at different wavelengths ($\lambda/L=0.8-1.2$, $H=120$ mm)

Fig. 23 shows the variation of impact pressure peaks of all monitoring points P1–12 on the bow flare and bottom areas in different wavelength cases ($\lambda/L=0.8-1.2$, $H=120$ mm). As seen from the curves, the largest peak pressure occurs at $\lambda/L=1.1$ for the majority of the monitoring points. Due to the pre-existing hydrostatic pressure of 2.33 kPa, the bow bottom pulsating pressures at P4, P8, and P12 are generally larger than the bow flare impact pressure, and the magnitude of pressure peak at P4, P8 and P12 are very close. Similarly, the bow flare impact pressure on the side area, i.e. at P5–7 and P9–11, show a similar trend with the bow bottom pulsating pressure, but with lower magnitudes. However, the bow flare impact pressure on the centerline, i.e. at P1–3, shows a large scatter especially at P1 and P3. This indicates that the bow flare slamming pressure especially on the front of the centerline is associated with stronger nonlinearity and randomness compared with the bow bottom pulsating pressure.

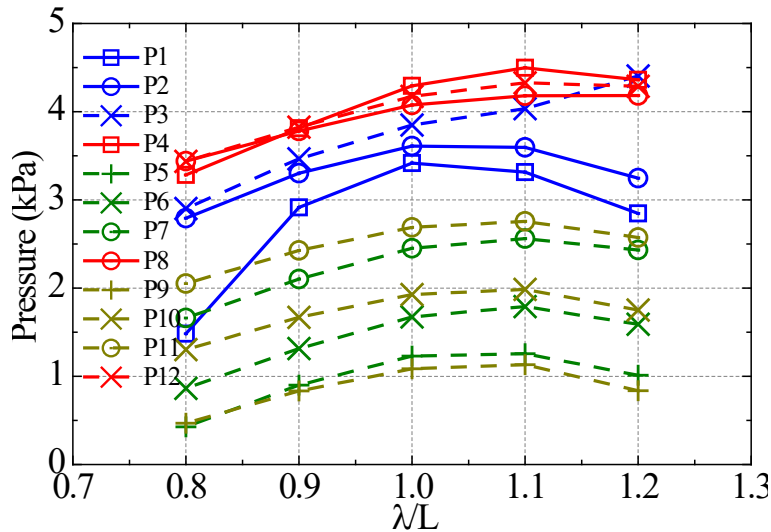


Fig. 23 Variation of the slamming pressure peaks with wavelength ($\lambda/L=0.8\text{--}1.2$, $H=120$ mm)

5.1.2 Varying with wave height

Visual observation of slamming events viewed from both top and underwater sides for the three wave steepness cases is compared in Fig. 24, where the same instant of time $t=9.05$ s when pronounced slamming and green water phenomena took place is selected. It is noted that the initial phase of the wave relative to the ship was set to be the same for the three different wave height cases in the CFD calculations. The figures show that the height of piling up water on the front deck increases with the increase of wave height and persists along the whole deck in higher wave cases ($H=180\text{--}240$ mm).

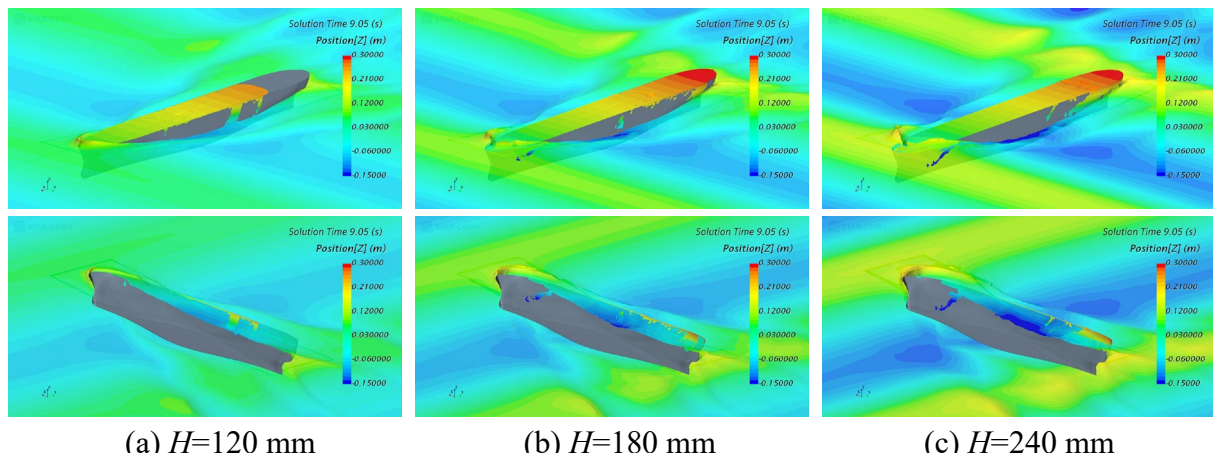


Fig. 24 Visual observation of the slamming event ($\lambda/L=1.2$, $H=120\text{--}240$ mm, $t=9.05$ s)

The time series of the impact pressure at typical positions, i.e. bow flare area measurement points P1–3 and bow bottom area measurement points P4, P8 and P12, in different wave height conditions ($\lambda/L=1.2$, $H=120\text{--}240$ mm) are compared in Fig. 25, where the results were low-pass filtered with a cut-off frequency of 450 Hz to remove noises.

As can be seen in the figure, the slamming pressure peak becomes higher and sharper with the increase of wave steepness. However, the duration of bow flare slamming at a specific point of P1–3 does not change much among different wave height cases. It is worth

mentioning that the peak pressure of P3 occurs at the water exit phase rather than the water entry phase due to its negative deadrise angle (inclined inward angle), which can be confirmed from the peak form especially in the high wave state. The peak pressure at P3 has the smallest difference between the values in different wave height cases among all the pressure measurement points.

In addition to the difference in peak values, the shape of the bow bottom impact pressure signal differs significantly among different wave height cases. The bow bottom area remains immersed in water at all times for the case of $H=120$ mm. However, it emerged from the water when the ship was in a bow up motion state in the higher wave state cases of $H=180\text{--}240$ mm. With the increase of wave height, the phenomenon of bow bottom pulsating pressure should be described by the bow bottom slamming impact since the bow bottom emerged from the water and re-entered into the water at a relatively high speed, which exceeds a threshold value corresponding to slamming occurrence. The zero pressure interval corresponds to the dry state of a specific point at the bow bottom. It is noted that the lowest pressure at the front of the bow bottom, point P4, is below zero. This can be explained by the fact of suction effect during a water exit process. The movement velocity of the bow bottom in the air made the pressure lower than the standard atmospheric pressure, which can be explained by the Bernoulli equation.

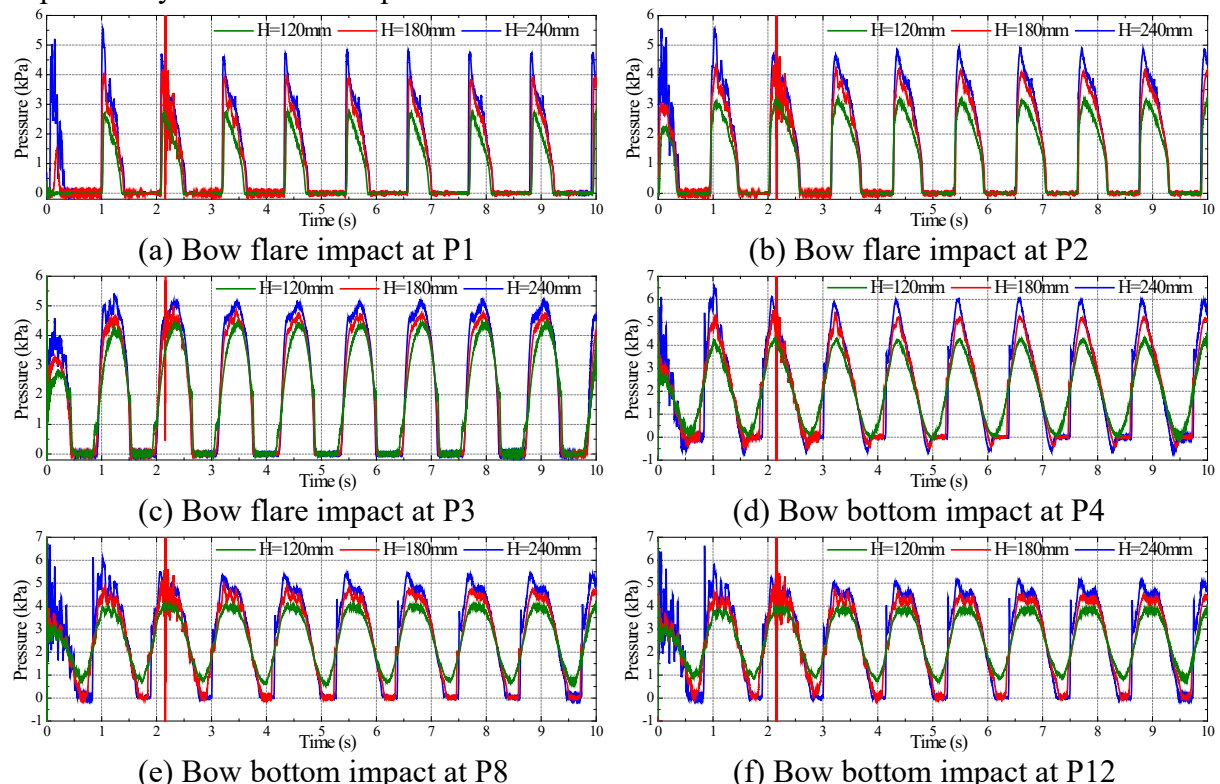


Fig. 25 Time series of typical slamming pressure at different wave heights ($\lambda/L=1.2$, $H=120\text{--}240$ mm)

Furthermore, it is observed from Fig. 25e–f that the pressure signal at P8 and P12 in high waves exhibit a triple-peak behaviour during each bow bottom slamming event. For a better observation and understanding of this phenomenon, the time series of the bow bottom

slamming pressure at P12 for the case of $H=240$ mm is shown in Fig. 26 with a locally enlarged view around one slamming peak. In the figure, both the original data and the low-pass filtered data with a cut-off frequency of 450 Hz are presented. It is observed that the bow bottom pulsating pressure signal oscillates significantly at adjacent samples especially around the peaks, which is mainly caused by the numerical errors induced during data exchange and mesh projection between the CFD and FEA solvers. However, the high-frequency noise components concentrate on the frequency range of 500 Hz which is far from the useful information.

The three peaks during one slamming event are marked with a black circle. According to Belik et al. (1988) and Guedes Soares (1989), the slamming force is assumed to be given by the sum of two components of impact slamming and momentum slamming. The first sharp peak with a small duration is caused by the initial impact of the bow bottom on the water surface. The second maximum peak with a longer rising time is mainly caused by the rate of change of the hydrodynamic momentum as the hull immerses into the water. The third peak is caused by the increase of hydrostatic pressure as the hull immerses into the water and the time instant of this peak corresponds to the critical state of bow downward and upward motions. This can be well explained from the pressure components analyzed in Section 6.4. A similar phenomenon is also reported in Huang et al. (2021b), who calculated the bow slamming pressure on the rigid body S175 ship model in cross-waves by pure CFD simulation. The sampling frequency of 1000 Hz used in this study is high enough to capture the impact peak, which can be confirmed from the locally enlarged view where the cross symbol denotes the original sampled data. Moreover, the calculated peak sharpness with a sampling frequency of 5000 Hz in the work of Huang et al. (2021b) is very similar to the present paper's result of 1000 Hz. However, the pressure signal oscillates in a certain range when the point is immersed into the water due to the numerical errors induced during data exchange and mesh projection between the CFD and FEA solvers. It is also noted that the small fluctuations on the crest of pressure curve in Figs. 25 and 26 are probably caused by the hydroelasticity effects.

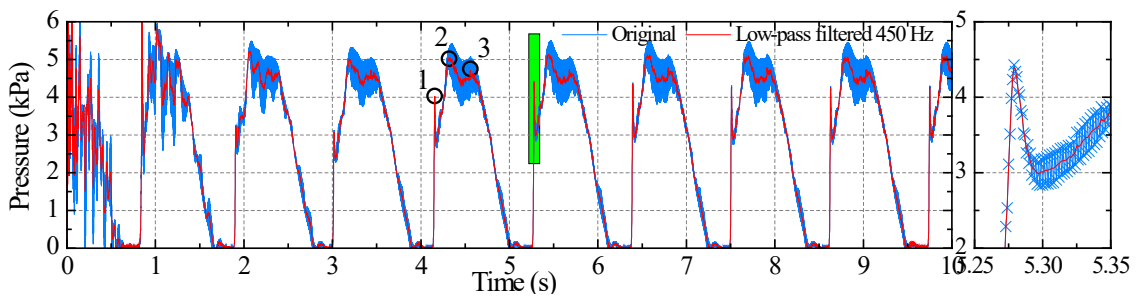


Fig. 26 Time series of bow bottom slamming pressure at P12 ($\lambda/L=1.2$, $H=240$ mm)

Fig. 27 shows the variation of impact pressure peaks at all the monitoring points P1–12 on both bow flare and bottom areas in different wave height cases. As seen from the curves, due to the pre-existing hydrostatic pressure of 2.33 kPa, the bow bottom pulsating pressure at P4, P8, and P12 are generally larger than the bow flare impact pressure for a specific wave height condition. The pressure increases almost linearly with the increase of wave height for

the majority of the points apart from P10. A notable phenomenon is that the pressure at P10 increases dramatically from $H=180$ mm to 240 mm.

To further analyze this notable phenomenon, a dedicated comparison of the bow flare impact pressure at P10 for different wave heights is comparatively shown in Fig. 28, where the results were low-pass filtered with a cut-off frequency of 450 Hz to remove noises. The results indicate that the peak sharpness increases dramatically with the increase of wave height and the sharp peak with a very small duration contributes more to the pressure at P10 in the high wave cases. It is known that the peak value of bow flare pressure is mainly determined by the water entry velocity, dead-rise angle and other geometrical parameters. The sharp peak at P10 in a high sea state is caused by the relatively low dead-rise angle in the large bow flare area and high vertical relative speed. A locally enlarged view around one peak is also inserted in each of the figures, which also confirms that the sampling frequency used is high enough to capture the impact peak.

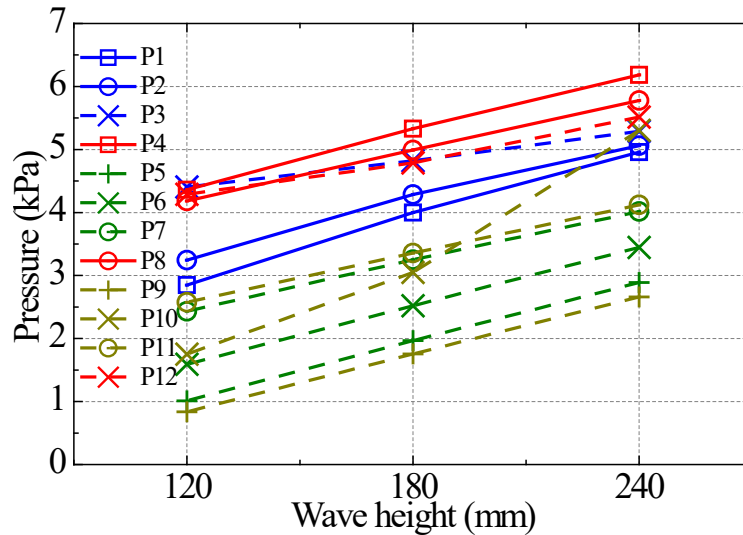
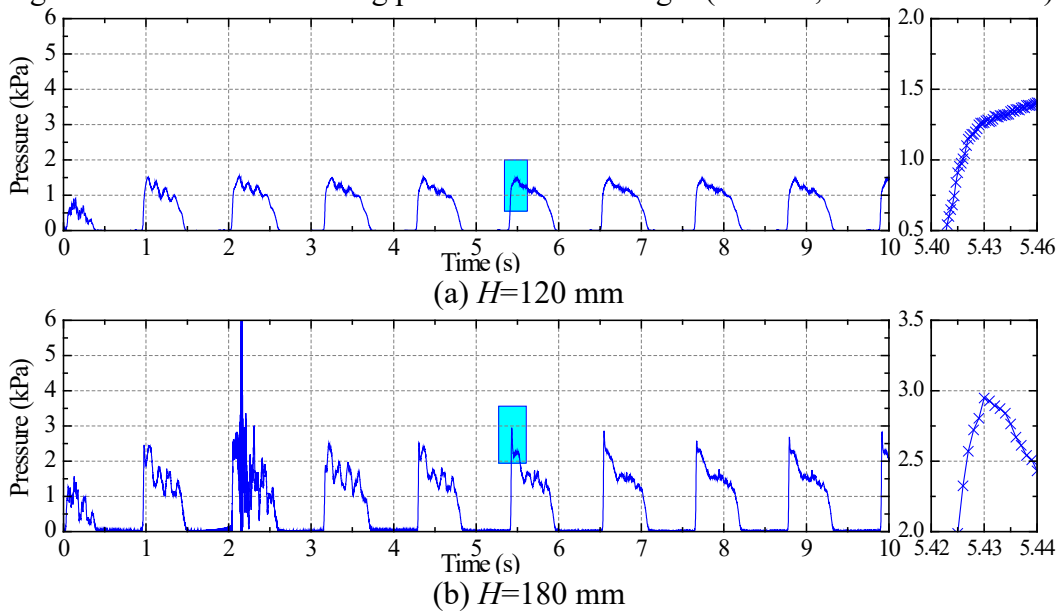


Fig. 27 Variation of slamming peaks with wave height ($\lambda/L=1.2$, $H=120$ – 240 mm)



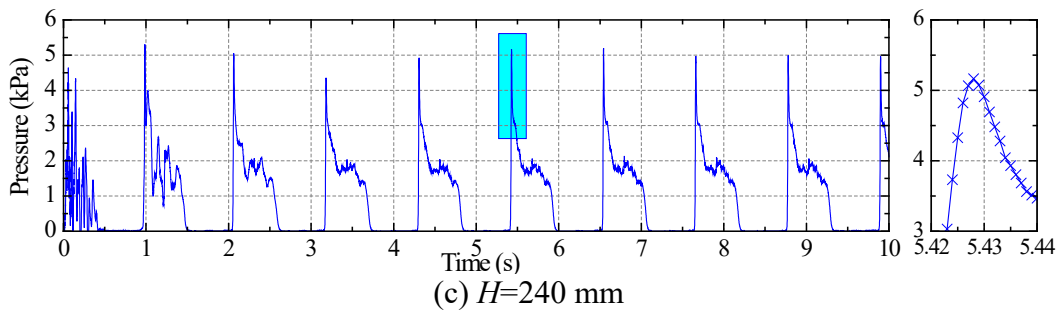


Fig. 28 Comparison of the bow flare impact pressure at P10 for different wave heights ($\lambda/L=1.2, H=120\text{--}240 \text{ mm}$)

5.2 Green water pressures on deck

5.2.1 Varying with wavelength

Green water on deck usually occurs followed by a bow flare slamming event when the waves are high or ship motions are large, or both. A comparison of the phenomenon of green water on deck for the ship sailing in different wavelength cases ($\lambda/L=0.8\text{--}1.2, H=120 \text{ mm}$) is made in Fig. 29. For the moderate wave height $H=120\text{mm}$ conditions, deck wetness only occurs in the cases of $\lambda/L=1.0\text{--}1.2$ due to relatively large ship vertical motions.

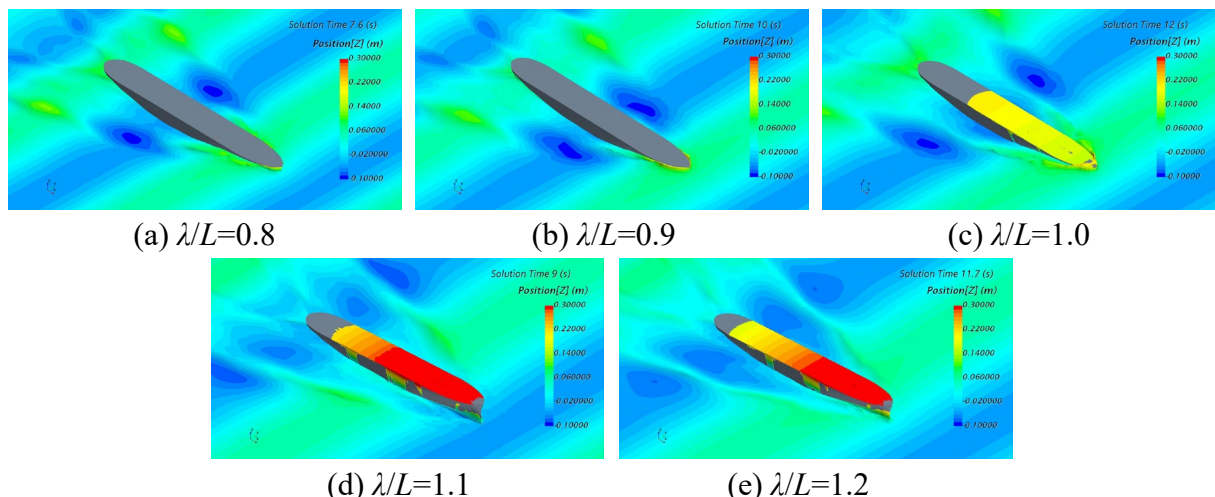


Fig. 29 Comparison of green water of ship in different wavelengths ($\lambda/L=0.8\text{--}1.2, H=120 \text{ mm}$)

The green water pressures on the centerline monitoring points D1, D3, D6, D9, D10, and D11 in these three conditions ($\lambda/L=1.0\text{--}1.2, H=120 \text{ mm}$) are shown in Fig. 30, where the results were low-pass filtered with a cut-off frequency of 450 Hz to remove noises. The results indicate that pronounced green water pressure can be only observed at D3 whereas the green water pressure at any other point is very weak. This can be explained by the fact that a mass of water overtopped the bow and impacted the front deck at D3 and then it splashed and dispersed during one shipping water event. For the case of $\lambda/L=1.0$, the pressure peak at D3 fluctuates significantly since the amount of shipping water is too small and it differs for individual green water events. The shipping water pressure peak at D3 is larger and relatively steady in the case of $\lambda/L=1.1$.

Fig. 31 shows the variation of the pressure peaks of all the monitoring points on deck D1–11 in different wavelength cases ($\lambda/L=0.8–1.2$, $H=120$ mm). As seen from the curves, the largest pressure peak occurs at $\lambda/L=1.1$ for the majority of the monitoring points, which show an agreement with the bow flare and bow bottom slamming pressure data in Fig. 23. For the measurement points P3–5 at the same transverse Station of 19.5, the impact pressure at P3 and P4 are comparable large, while P5 which is located near the edge of the deck is much lower.

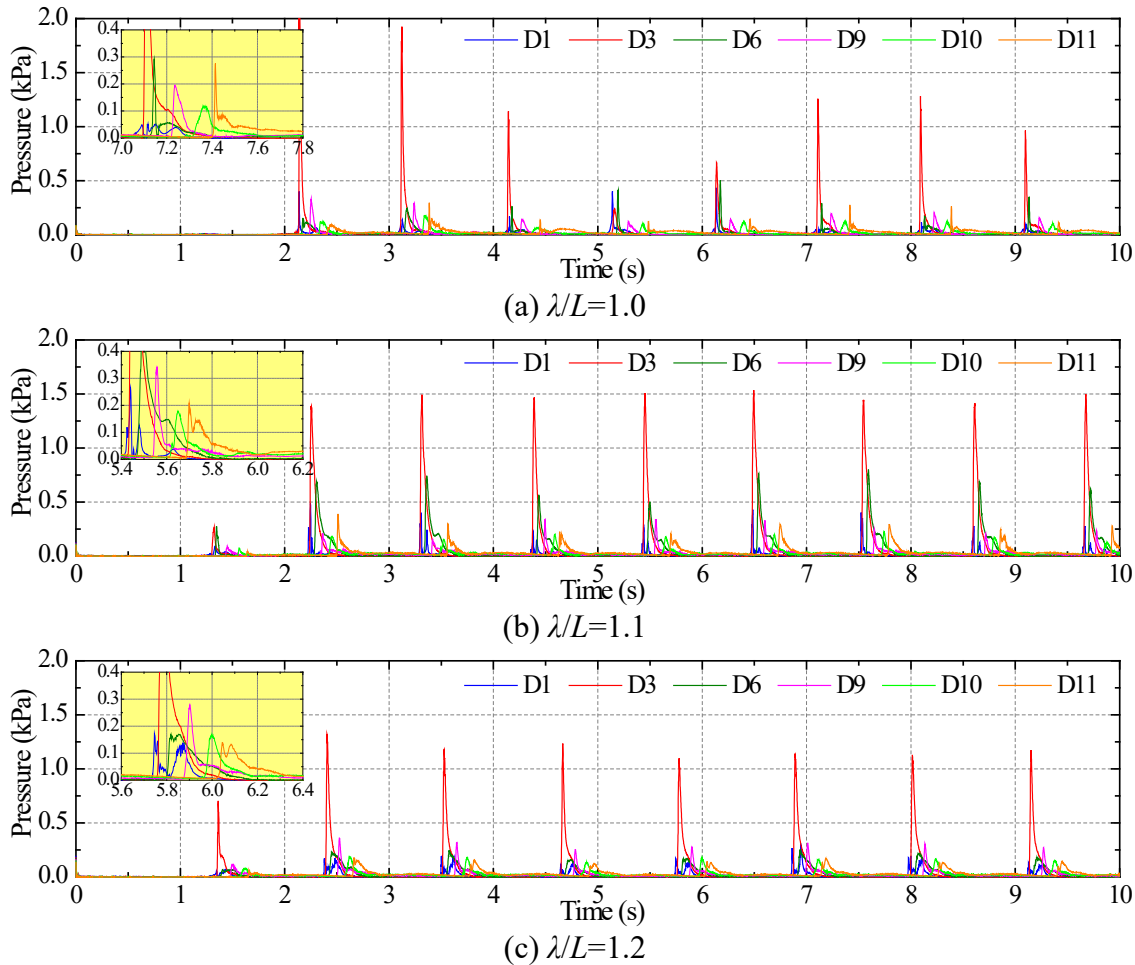


Fig. 30 Time series of green water pressure at different wavelengths ($\lambda/L=1.0–1.2$, $H=120$ mm)

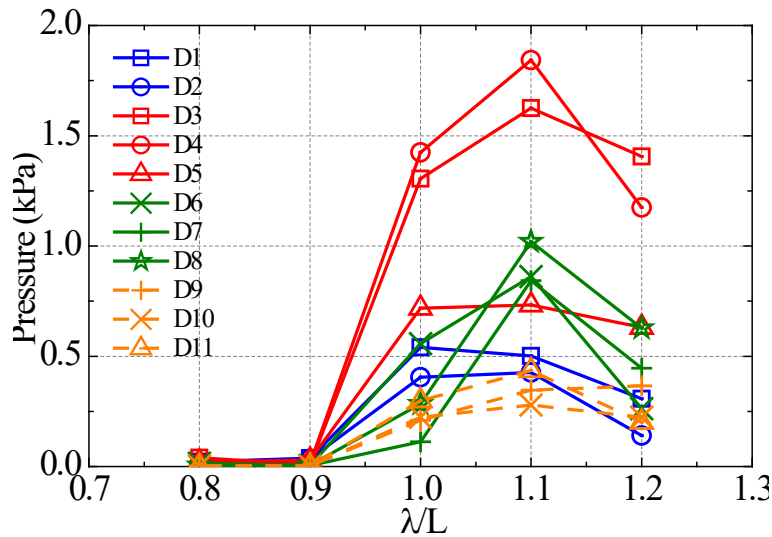


Fig. 31 Variation of green water pressure with wavelength ($\lambda/L=0.8\text{--}1.2$, $H=120$ mm)

5.2.2 Varying with wave height

Visual observation of the wave pattern and green water on deck phenomenon for the three wave height cases at the same instant of time $t=8.2$ s is compared in Fig. 32. The green water pressures on the centerline monitoring points D1, D3, D6, D9, D10, and D11 in different wave height conditions ($\lambda/L=1.2$, $H=120\text{--}240$ mm) are compared in Fig. 33, where the results were low-pass filtered with a cut-off frequency of 450 Hz to remove noises. The results indicate that the green water pressures in high wave states of $H=180$ mm and 240 mm are more severe than in the moderate wave height of $H=120$ mm. In the moderate sea wave condition ($H=120$ mm) obvious green water pressure only occurs at D3. However, in severer wave conditions ($H=180$ and 240 mm) the impact pressures at areas in front of Station 19, i.e. at D1, D3, and D6, are all pronounced although the pressure trends to weaken downstream, i.e. at D9–11 which are located behind Station 19. Moreover, the peak becomes sharper with the increase of wave height due to the increase of impact velocity.

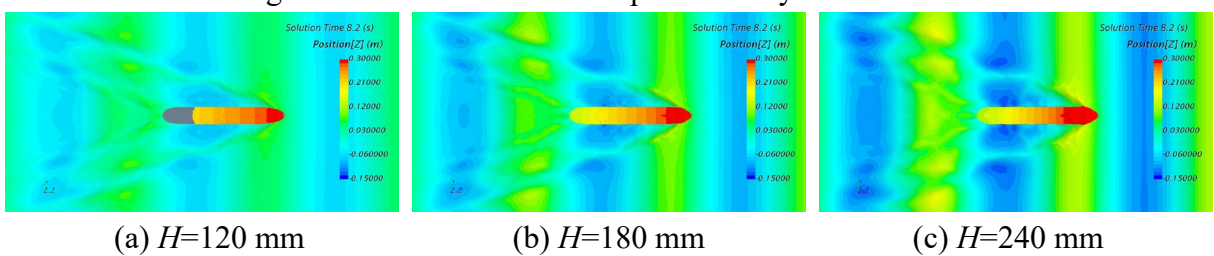
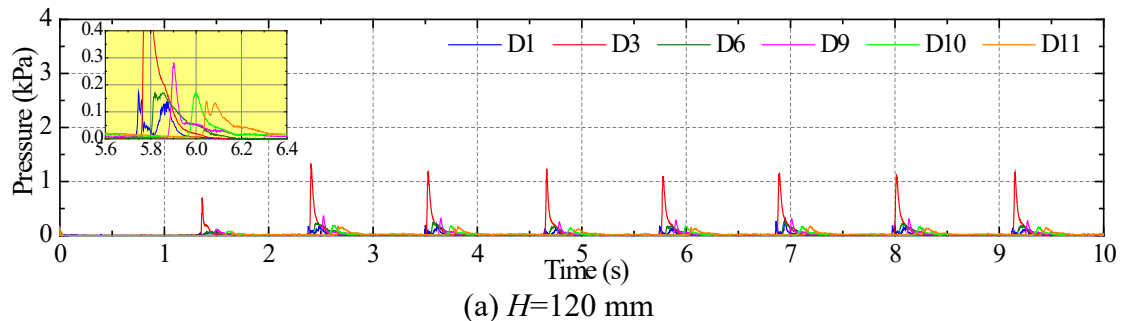


Fig. 32 Visual observation of the green water on deck ($\lambda/L=1.2$, $H=120\text{--}240$ mm, $t=8.2$ s)



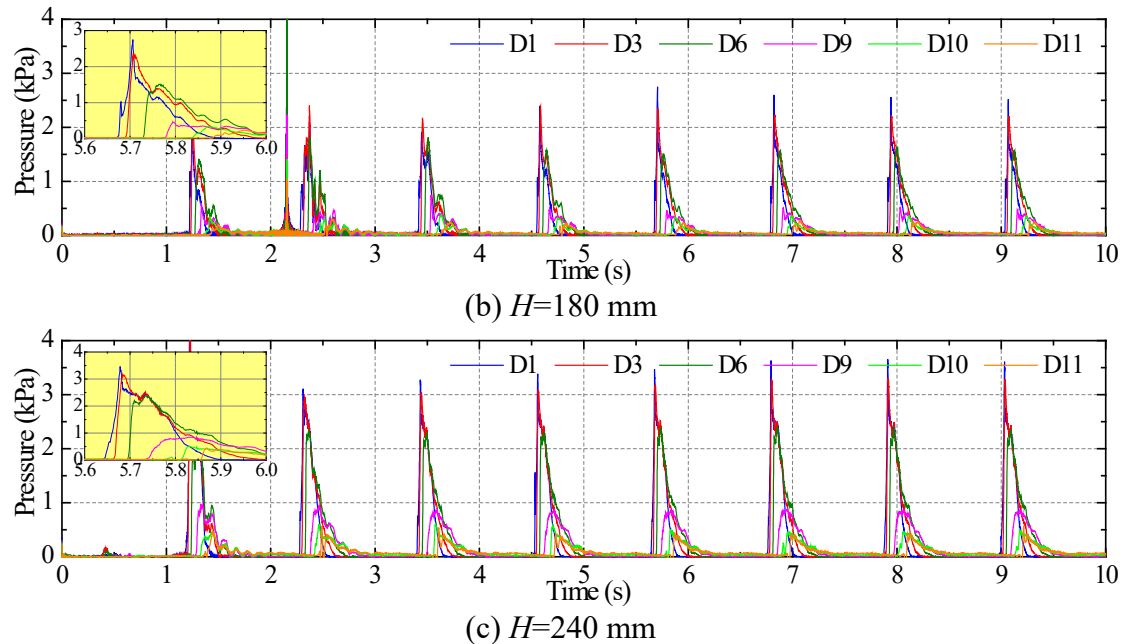


Fig. 33 Time series of green water pressure at different wave heights ($\lambda/L=1.2$, $H=120\text{--}240$ mm)

Fig. 34 shows the variation of the green water pressures of all the monitoring points on deck D1–11 in different wave height cases. As seen from the curves, the pressure peak increases with the increase of wave height for all the cases. The rate of increase is small for the range from $H=180$ mm to 240 mm compared with that from $H=120$ mm to 180 mm for the majority of the points apart from D9–11. It is also found that the impact pressure at D5 is much lower than D3 and D4 although they are located at the same cross-section even in the higher wave condition. To further investigate this notable phenomenon, a direct comparison of the time series of pressure at D3–5 in the severest wave condition ($\lambda/L=1.2$, $H=240$ mm) is shown in Fig. 35. The results indicate that the difference in the impact peak is mainly caused by the instantaneous sharp peak while the overall profile and impact duration, which represents the rate of change of hydrodynamic momentum as the front deck immerses into the water, show a good agreement among the different cases.

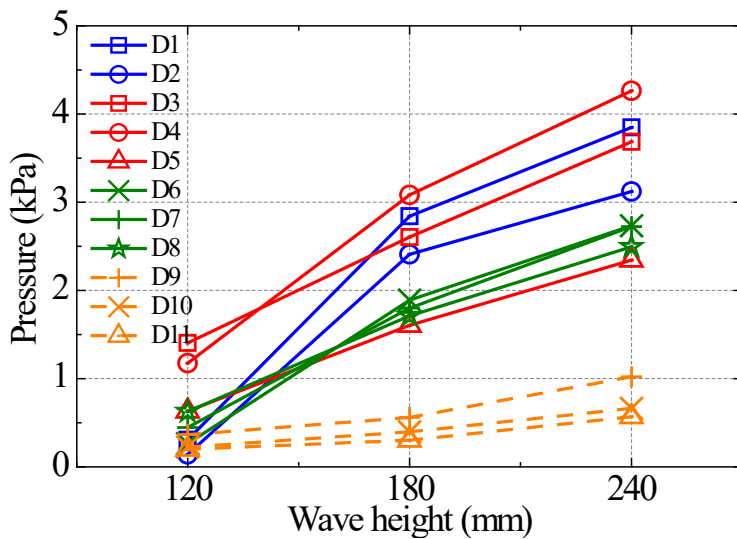


Fig. 34 Variation of green water pressures with wave height ($\lambda/L=1.2$, $H=120\text{--}240$ mm)

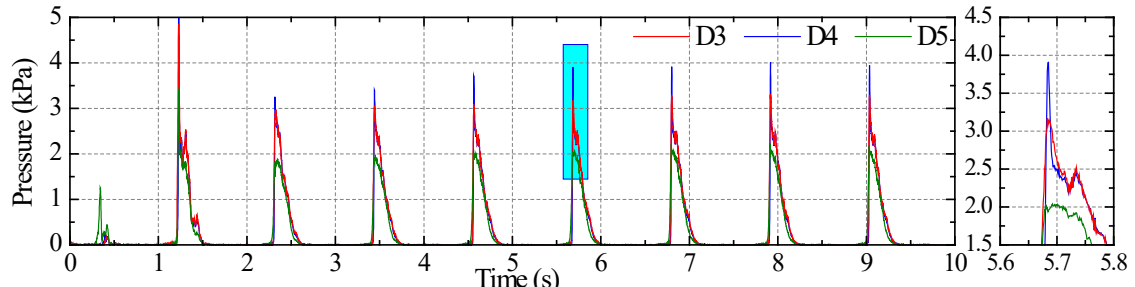


Fig. 35 Comparison of green water pressures at different transverse positions at Station 19.5 ($\lambda/L=1.2$, $H=240$ mm)

6. Simplified method for slamming pressure estimation

Since the capture of slamming pressure peak requires a very high iteration and sampling frequency (small time step), it is very time-consuming to calculate the slamming pressure by using the coupled CFD–FEA method. To overcome this limitation, a simplified slamming pressure estimation method by using the ship–wave relative movement data is proposed, which could largely reduce the computation burden of the two-way CFD–FEA FFSI simulations. The estimated time series of bow flare and bow bottom slamming pressure is sufficient for engineering application accuracy.

In the proposed simplified method, the slamming pressure (p) is assumed to be the sum of two pressure components that have already been identified by Guedes Soares (1989). The first is an impact component (p_I) related to the impact of the bow bottom or bow flare with the water and characterized by a large peak with a small duration. The second component (p_S) is caused by the hydrostatic pressure as it varies with the change of hull immersed depth in water.

$$p = p_I + p_S \quad (6)$$

According to Stavovy and Chuang (1976), the impact pressure can be determined by the

following equation:

$$p_I = \frac{1}{2} \rho K V^2 \quad (7)$$

where ρ denotes fluid density, K denotes impact pressure factor which mainly depends on the sectional shape especially the local dead-rise angle at a specific point considered, V denotes vertical relative speed between the ship structure and the wave. In the present method, the impact pressure during the whole water entry procedure is estimated by the above equation.

The hydrostatic pressure is simply determined by the immersed depth of the point on the hull surface considered using the following equation:

$$p_S = \rho g h \quad (8)$$

where g denotes gravity acceleration, h denotes the immersed depth from the wave surface.

6.1 Estimation of the impact pressure factor

The impact pressure factor K can be regarded as constant and is independent of sea severity and impact speed. The value of K can be determined by different methods such as empirical formula (Ochi and Motter, 1973), Rule Book approach (Lloyd's Register, 2011), experiments (Wang and Guedes Soares, 2016b) and numerical simulation (Wang and Guedes Soares, 2013; Yu et al., 2018).

The simplest method to obtain the impact pressure factor at bow flare area includes applying the empirical formula proposed by von Karman (1929) and Wagner (1932), which are, respectively, expressed as follows:

$$K = \frac{\pi}{\tan \chi} \quad (9)$$

$$K = 1 + \frac{\pi^2}{4 \tan^2 \chi} \quad (10)$$

where χ denotes dead-rise angle at a specific point. The estimated impact pressure factors for P9 and P10 on Station 19 by the two empirical formula methods are summarized in Table 6.

Table 6 The obtained impact pressure factor at bow flare area

Point	P9	P10
Dead-rise angle (°)	49	59
von Karman method	2.730	1.888
Wagner method	2.863	1.891
Mean	2.797	1.890

Moreover, to obtain the impact pressure factor at the bow bottom area, the CFD software STAR-CCM+ is used to simulate the water entry process of a 2D hull section and record its vertical speed and the impact pressure at points of interest (see Fig. 36). Thus the slamming pressure coefficients at bow bottom P12 on the hull section can be obtained by applying the inverse operation of Eq.(7) and substituting the impact pressure peak and its corresponding

speed. In this study, the cross-section at Station 19 is subjected to free-falling and water entry at three different heights of 1 m, 2 m and 3 m (corresponding to the initial speed of 4.429 m/s, 6.264 m/s and 7.672 m/s, respectively). The obtained pressure at P12 and vertical speed for different initial heights are summarized in Fig. 37. The estimated impact pressure factors for P12 are summarized in Table 7. It is noted that the sampling frequency may affect the peak value of slamming pressure if the sampling frequency is not sufficient, while its influence on the vertical speed is relatively small. In this case, the sampling frequency was set at 1000 Hz which is the same as that used in the CFD–FEA co-simulations.

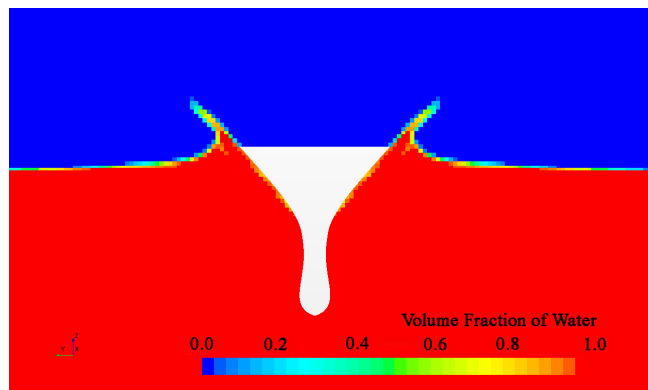


Fig. 36 Simulation of water entry process of 2D hull section of Station 19

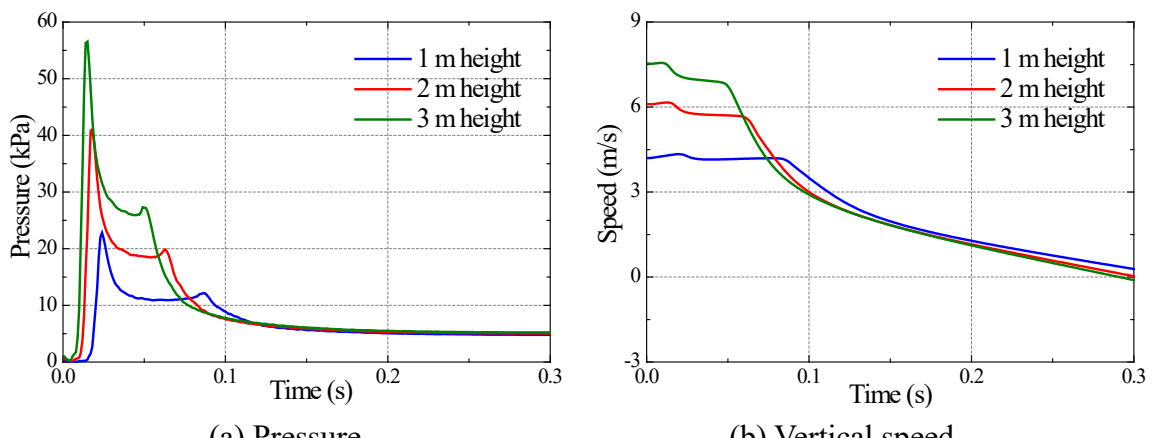


Fig. 37 The calculated time series of pressure and speed

Table 7 The obtained impact pressure factor at P12

Initial height (m)	Peak pressure (kPa)	Speed (m/s)	K
1	22.736	4.284	2.478
2	41.136	6.072	2.231
3	56.399	7.410	2.054
Mean			2.254

6.2 Vertical relative speed between ship and wave

To calculate the impact pressures between the ship hull and the wave surface it is necessary to obtain their relative vertical velocity, which can be directly obtained from the seakeeping results of ship motions and wave elevation. Without loss of generality, the relative motion displacement or speed relative to the wave surface for a ship operating in regular waves at any heading angle can be obtained in the following way.

The vertical motion displacement at a specific point $Q (x_b, y_b, z_b)$ on the hull surface in real-time can be estimated by:

$$z_Q(t) = z - x_b \sin \theta - y_b \sin \varphi \quad (11)$$

where z, φ, θ denotes ship heave, roll and pitch motion displacement in real-time, respectively. Note that the coordinate position of $Q (x_b, y_b, z_b)$ is described in the plane movement system, whose origin coincides with the centre of gravity of the ship.

The corresponding vertical motion speed of the specific point on the hull can be obtained by acquiring the time derivative of the displacement:

$$v_Q(t) = \dot{z} - x_b \dot{\theta} \cos \theta - y_b \dot{\varphi} \cos \varphi \quad (12)$$

According to the linear seakeeping theory, the hull heave, roll and pitch motion in regular waves can be represented by:

$$\begin{cases} z(t) = R_z \zeta_a \cos(\omega_e t + \varepsilon_z) \\ \varphi(t) = R_\varphi \zeta_a \cos(\omega_e t + \varepsilon_\varphi) \\ \theta(t) = R_\theta \zeta_a \cos(\omega_e t + \varepsilon_\theta) \end{cases} \quad (13)$$

where ζ_a denotes wave amplitude, ω_e denotes wave encounter frequency, R_z, R_φ, R_θ denote the response amplitude of ship heave, roll and pitch motions under unit wave amplitude, respectively; $\varepsilon_z, \varepsilon_\varphi, \varepsilon_\theta$ denote the initial phase of ship heave, roll and pitch motions, respectively.

The longitudinal position of the specified point $Q (x_b, y_b, z_b)$ along the wave propagation direction in the earth fixed coordinate system is expressed as:

$$X = (U t + x_b) \cos \beta - y_b \sin \beta \quad (14)$$

where U denotes the ship forward speed, β denotes a wave heading angle.

The wave elevation at the specified point $Q (x_b, y_b, z_b)$ is expressed as:

$$\zeta(X, t) = \zeta_a \cos \{\omega_e t + k[(U t + x_b) \cos \beta - y_b \sin \beta]\} \quad (15)$$

where k denotes the wavenumber. The vertical speed of the wave surface can be obtained by acquiring the time derivative of the wave elevation:

$$v_\zeta(t) = -\zeta_a (\omega_e + k U \cos \beta) \sin \{\omega_e t + k[(U t + x_b) \cos \beta - y_b \sin \beta]\} \quad (16)$$

The relative vertical displacement and speed between the ship section where the specified point $Q (x_b, y_b, z_b)$ locates and the wave surface is, respectively, given by:

$$w(t) = z_Q(t) - \zeta(t) \quad (17)$$

$$v(t) = v_Q(t) - v_\zeta(t) \quad (18)$$

An example of the relative vertical motion displacement and speed of ship section at Station 19 with respect to the wave surface obtained from the CFD–FEA co-simulation in the typical condition ($\lambda/L=1.2$, $H=240$ mm) is shown in Fig. 38. It is noted that the incident wave elevation at Station 19 is the theoretical data of the 5th Stokes wave. The vertical speed is obtained by acquiring the time derivative of the adjacent motion displacement using the discrete data.

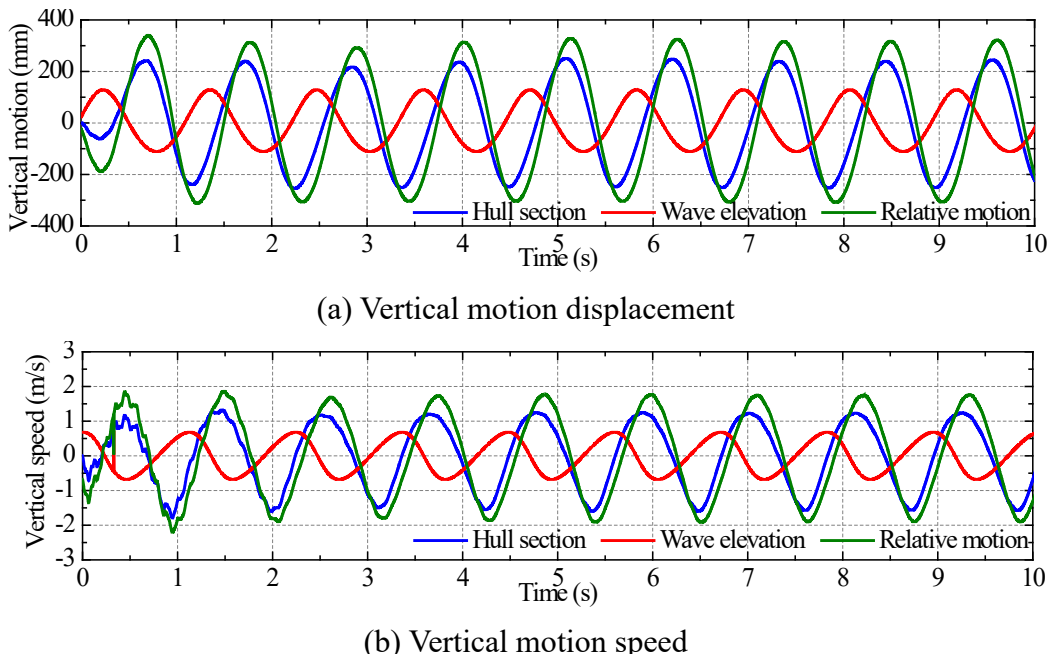


Fig. 38 Relative motion of ship section at Station 19 with wave surface ($\lambda/L=1.2$, $H=240$ mm)

6.3 Identification of slamming duration

Severe bow bottom slamming occurs when vertical ship motions tend to be large, while the bow bottom fluctuation pressure always exists even in a low wave sea state. On the other hand, bow flare slamming occurs only when both of the two conditions are met: the relative velocity is larger than the critical value and the relative motion is larger than the vertical distance from the still water surface to the specific point. The relative position of a specific point on the hull surface with respect to the wave surface can be obtained by Eq.(17). A point on the hull surface above the waterline is in a wetted condition when the relative motion displacement exceeds the vertical distance from the still water surface to the point.

Moreover, a point can be in either a water entry phase or water exit phase when it is immersed in the water. In this study, it is assumed that the water impact only occurs when the point is in the water entry phase while the impact pressure is zero in the water exit phase as the converse relative speed does not cause an impact pressure. The water entry or water exit phase can be identified from the increasing interval or decreasing interval of the absolute value of relative motion displacement, respectively.

Fig. 39 shows an example of the identification of slamming events at bow flare area

point P10 in the typical high wave condition ($\lambda/L=1.2$, $H=240$ mm). In Fig. 39a the curve corresponds to the relative vertical motion displacement between a ship section and wave given in Fig. 38a. The green horizontal line denotes the critical value that the ship is in a motion state when the pressure point P10 coincides with the alternate dry and wet water surface. The relative motion curve below the critical value plotted by the red curve corresponds to the duration that the point P10 is in a wet condition including both the water entry and water exit phases. On the time series of the relative vertical motion, the beginning of the water entry phase, end of slamming impact and end of the water exit phase is marked by black, purple and orange circles, respectively. Fig. 39b shows the corresponding relative vertical speed with marks of the beginning and end time of each slamming event as determined in Fig. 39a. To better understand the ship wave relative motion state at a typical time, Fig. 40 shows the incident wave profile along the ship length in the three typical motion states of the ship within one slamming event.

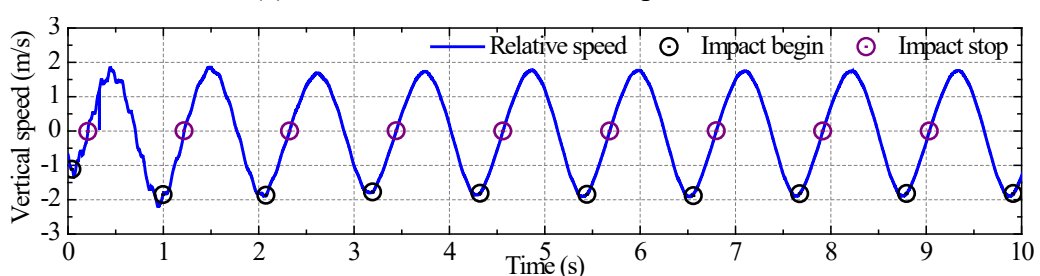
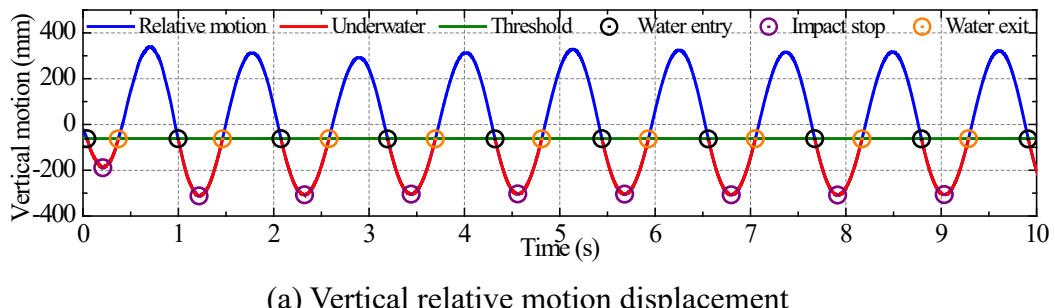
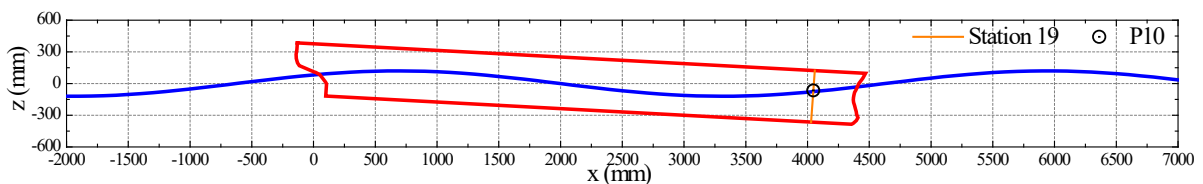
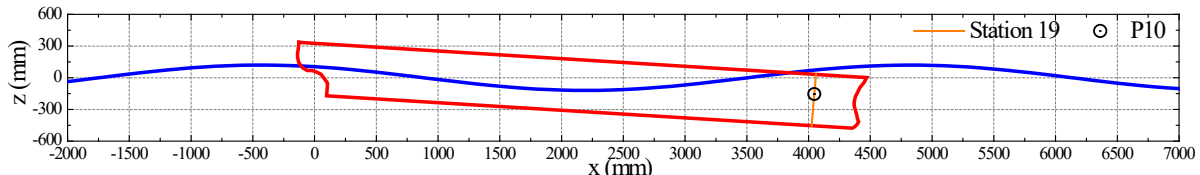
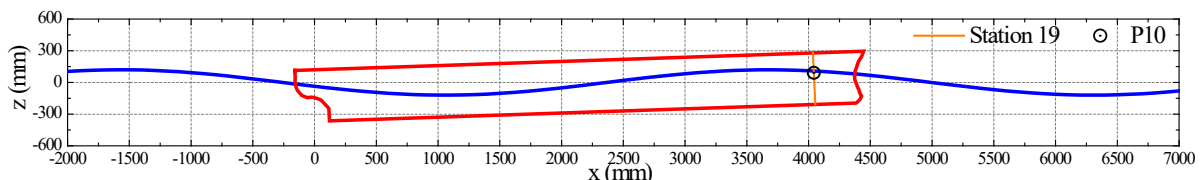


Fig. 39 Identification of slamming event at bow flare area P10 ($\lambda/L=1.2$, $H=240$ mm)





(b) The end of slamming impact phase of P10 ($t=4.561$ s)



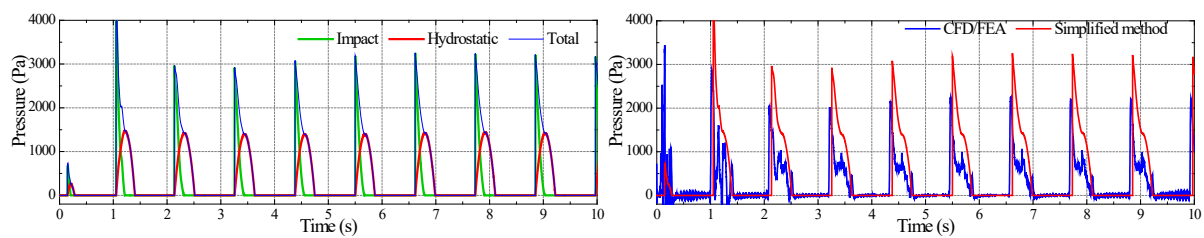
(c) The end of water exit phase of P10 ($t=4.810$ s)

Fig. 40 Wave profile along the ship length in typical ship motion states ($\lambda/L=1.2$, $H=240$ mm)

6.4 Validation of the simplified method

The predicted time series of the slamming pressure including the impact pressure and hydrostatic pressure components by the simplified method at three typical points (i.e. bow flare area P9–10 and bow bottom area P12) in the high and moderate wave states ($\lambda/L=1.2$, $H=180$ – 240 mm) are shown in Fig. 41 and 42, where the estimated slamming pressure signals are also compared with the direct calculation data by the coupled CFD–FEA method.

The results indicate that the estimated impact pressure generally shows a good agreement with the direct calculation results in both the peak value and duration, which satisfies the engineering application accuracy. The inclusion of the hydrostatic pressure component in the total slamming pressure turns out to be useful, which is however not considered in most existing methods. The difference in the results between the simplified method and direct calculation may be caused by various reasons such as the pitch motion, which affects the deadrise angle, which is not considered in this study. Moreover, the horizontal impact speed component caused by ship forward speed and 3D geometric variations along the longitudinal direction is neglected. It is also worth mentioning that the K value has a significant influence on the predicted results of pressure peak by the simplified method. Thus, the difference and sensitivity of K value by different methods should also be concerned.



(a) Pressure components at P9

(b) Comparison of results at P9

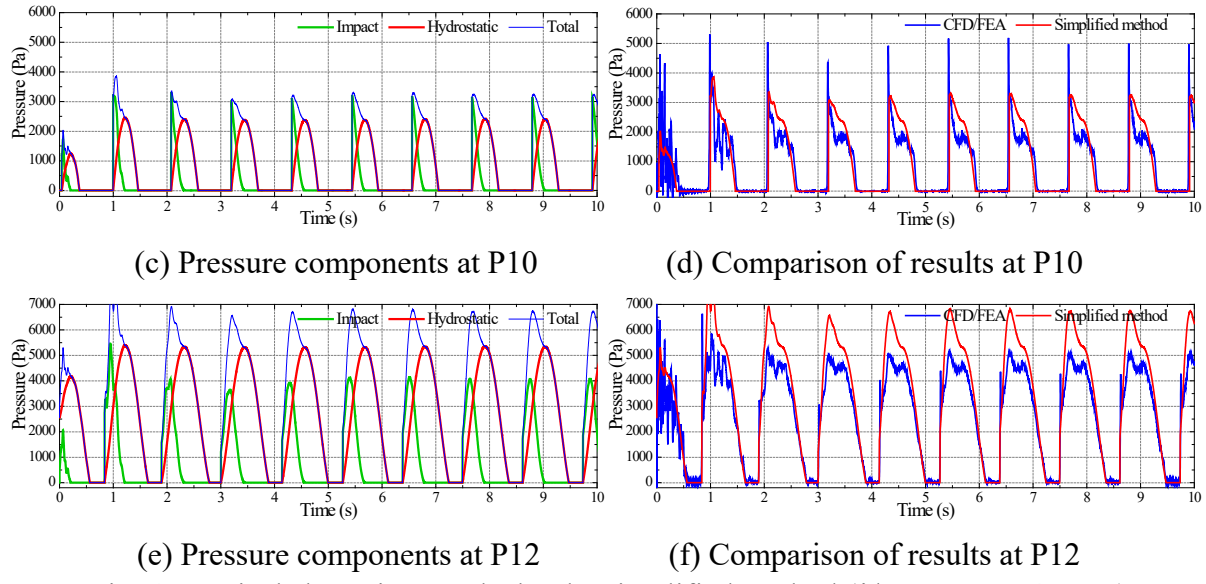


Fig. 41 Typical slamming results by the simplified method ($\lambda/L=1.2$, $H=240 \text{ mm}$)

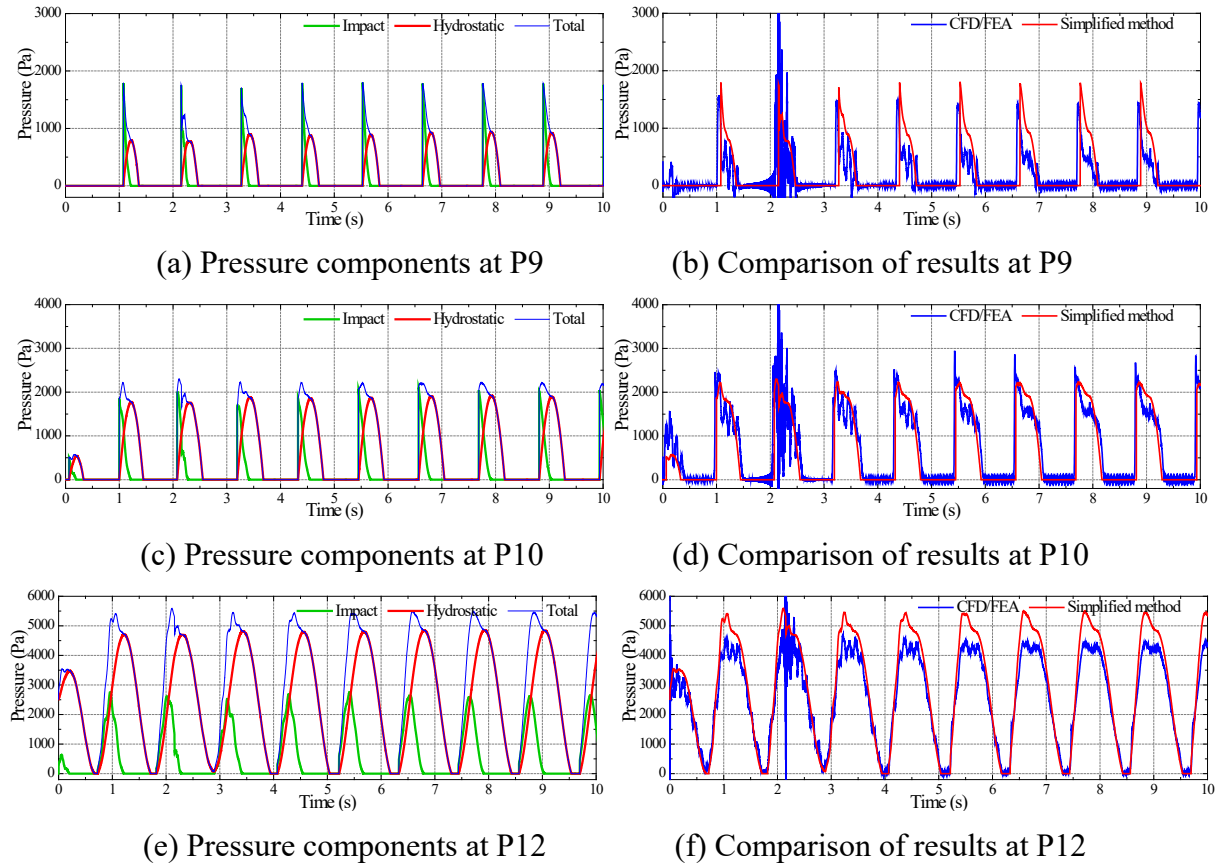


Fig. 42 Typical slamming results by the simplified method ($\lambda/L=1.2$, $H=180 \text{ mm}$)

7. Conclusions

In this study, a two-way coupled CFD–FEA simulation approach for the prediction of ship wave loads and slamming loads considering hydroelastic effects with a forward speed is developed and implemented on a flexible S175 containership model. The following

conclusions can be drawn based on this study:

(1) The two-way coupled CFD–FEA method is capable of simulating the seakeeping, wave loads, whipping responses, slamming and green water pressures of a flexible ship sailing in regular waves. The slamming and green water pressures are satisfactorily reproduced with fewer assumptions by using the coupled CFD–FEA method when compared to other methods, which is rarely reported in existing publications but has wide and significant potential.

(2) Formal convergence studies on the grid density and time step size have been conducted which show oscillatory convergence or oscillatory convergence is observed for ship motions and slamming pressures. However, the high-frequency whipping responses in VBM simulated by the coupled CFD–FEA method are not as steady as other signals such as the motions and impact pressures. The slamming pressure signal for a panel immersed in water oscillates in a certain range, which is caused by the numerical oscillation during data exchange and mesh projection between the CFD and FEA solvers.

(3) The hull flexibility can slightly affect the pulsating pressure which lasts for a longer period by posing high-frequency vibrations at the crest of the pressure curve. However, the influence of hull flexibility on the surface impact pressure is ignorable, especially for the transient impact pressure. The reasons are that the wave-induced structural deformation of the hull girder is very small for a 175-meter-long ship prototype with normal stiffness as well as the elastic deformation of the hull surface due to external fluid pressure is suppressed in this study.

(4) The simplified method for slamming pressure estimation predicts the slamming peak value and duration well, and the results show acceptable agreement with the direct calculation data by the coupled CFD–FEA method. The inclusion of hydrostatic pressure component in total slamming pressure estimation turns out to be useful, which is however not considered in the majority of existing methods. The simplified method of slamming pressure estimation will be useful and helpful in reducing the computation burden of the CFD–FEA co-simulations. However, it is worth mentioning that the present simplified formula does not include hull flexibility effects, thus its applicability to large container ships with more flexible hull structures needs further investigation.

Acknowledgements

This research is supported by the National Natural Science Foundation of China (No. 51909096), the Guangdong Basic and Applied Basic Research Foundation (No. 2020A1515011181) and the Science and Technology Program of Guangzhou, China (No. 202102020899). This work contributes to the Strategic Research Plan of the Centre for Marine Technology and Ocean Engineering (CENTEC), which is financed by the Portuguese Foundation for Science and Technology (Fundação para a Ciência e Tecnologia - FCT) under contract UIDB/UIDP/00134/2020. The first author would also like to thank the China Scholarship Council (CSC) for the financial support of his one-year visit to the CENTEC at the University of Lisbon.

References

- Bakica A, Malenica S, Vladimir N, 2020. Hydro-structure coupling of CFD and FEM - Quasi-static approach. *Ocean Engineering*, 217, 108118.
- Belik O, Bishop RED, Price WG, 1988. Influence of bottom and flare slamming on structural responses. *Transactions RINA*, 130: 325–337.
- Bishop RED, Price WG , 1979. *Hydroelasticity of Ships*. Cambridge University Press.
- Camilleri J, Taunton DJ, Temarel P, 2018. Full-scale measurements of slamming loads and responses on high-speed planing craft in waves. *Journal of Fluids and Structures*, 81: 201–229.
- Chen RZ, Du SX, Wu YS, Lin JR, Hu JJ, Yue YL, 2001. Experiment on extreme wave loads of a flexible ship model, In: Practical Design of Ships and Other Floating Structures. Proceedings of the Eighth International Symposium on Practical Design of Ships and Other Floating Structures, Shanghai, China, 2001-9-16 to 2001-9-21, 2001, pp. 871–878.
- Datta R, Guedes Soares C, 2020. Analysis of the hydroelastic effect on a container vessel using coupled BEM-FEM method in the time domain. *Ships & Offshore Structures*, 15(4): 393–402.
- Fonseca N, Guedes Soares C, 2004. Experimental investigation of the nonlinear effects on the vertical motions and loads of a containership in regular waves. *Journal of Ship Research*, 48(2): 118–147.
- Fonseca N, Guedes Soares C, 2005. Experimental investigation of the shipping of water on the bow of a containership. *Journal of Offshore Mechanics and Arctic Engineering*, 127(4): 322–330.
- Guedes Soares, C., 1989. Transient response of ship hulls to wave impact. *International Shipbuilding Progress*, 36(406): 137-156.
- Guedes Soares C, Pascoal R, Antao E, Voogt A, Buchner B, 2007. An approach to calculate the probability of wave impact on a FPSO bow. *Journal of Offshore Mechanics and Arctic Engineering*, 129(2): 73–80.
- Hirdaris SE, Bai W, Dassi D, Ergin A, Gu X, Hermundstad OA, Huijsmans R, Iijima K, Nielsen UD, Parunov J, Fonseca N, Papanikolaou A, Argyriadis K, Incecik A, 2014. Loads for use in the design of ships and offshore structures. *Ocean Engineering*, 78: 131–174.
- Hermundstad OA, Moan T, 2005. Numerical and experimental analysis of bow flare slamming on a Ro–Ro vessel in regular oblique waves, *Journal of Marine Science and Technology*, 10: 105–122.
- Huang SX, Jiao JL, Guedes Soares C, 2021a. Uncertainty analysis on the CFD–FEA co-simulations of ship wave loads and whipping responses. *Marine Structures*, (Under review).
- Huang SX, Jiao JL, Chen CH, 2021b. CFD prediction of ship seakeeping behavior in bi-directional cross wave compared with in uni-directional regular wave. *Applied Ocean*

Research, 107, 102426.

ITTC, 2017. Recommended Procedures and Guidelines, 7.5-03-01-01, Uncertainty Analysis in CFD Verification and Validation Methodology and Procedures.

ITTC, 2011. Recommended Procedures and Guidelines: Practical Guidelines for Ship CFD Applications.

Jiao JL, Ren HL, 2016. Characteristics of bow-flare slamming and hydroelastic vibrations of a vessel in severe irregular waves investigated by segmented model experiments. *Journal of Vibroengineering*, 18(4): 2475–2494.

Jiao JL, Yu HC, Chen CH, Ren HL, 2019. Time-domain numerical and segmented model experimental study on ship hydroelastic responses and whipping loads in harsh irregular seaways. *Ocean Engineering*, 185: 59–81.

Jiao JL, Chen ZY, Chen CH, Ren HL, 2020. Time-domain hydroelastic analysis of nonlinear motions and loads on a large bow flare ship in high irregular seas. *Journal of Marine Science and Technology*, 25(2): 426–454.

Jiao JL, Huang SX, 2020. CFD simulation of ship seakeeping performance and slamming loads in bi-directional cross wave. *Journal of Marine Science and Engineering*, 8(5), 312.

Jiao JL, Huang SX, Wang S, Guedes Soares C, 2021a. A CFD–FEA two-way coupling method for predicting ship wave loads and hydroelastic responses. *Applied Ocean Research*, (Under review).

Jiao JL, Huang SX, Guedes Soares C, 2021b. Viscous fluid–flexible structure interaction analysis on ship springing and whipping responses in regular waves. *Journal of Fluids and Structures*, 106, 103354.

Jiao JL, Huang SX, Guedes Soares C, 2021c. Numerical simulation of ship motions in cross waves using CFD. *Ocean Engineering*, 223, 108711.

Kim JH, Kim Y, Yuck RH, Lee DY, 2015. Comparison of slamming and whipping loads by fully coupled hydroelastic analysis and experimental measurement. *Journal of Fluids and Structures*, 52: 145–165.

Lakshmynarayana PAK, Hirdaris S, 2020. Comparison of nonlinear one- and two-way FFSI methods for the prediction of the symmetric response of a containership in waves. *Ocean Engineering*, 203, 107179.

Lakshmynarayana PA, Temarel P, 2020. Application of a two-way partitioned method for predicting the wave-induced loads of a flexible containership. *Applied Ocean Research*, 96, 102052.

Li ZF, Ren HL, Liu RM, Li H, 2017. Time domain Rankine-Green panel method for offshore structures. *Journal of Ocean University of China*, 16(1): 65–73.

Lin Y, Ma N, Gu XC, Wang DY, 2020. Experimental study on the asymmetric impact loads and hydroelastic responses of a very large container ship. *International Journal of Naval Architecture and Ocean Engineering*, 12: 226–240.

Lin Y, Ma N, Gu XC, 2021. Potential-flow and CFD investigations of bow-flare slamming on a container ship in regular heading waves. *Ocean Engineering*, 219, 108278.

- Lloyd's Register, 2011. General Information for the Rules and Regulations for the Classification of Naval Ships.
- Luo HB, Wang H, Guedes Soares C, 2012. Numerical and experimental study of hydrodynamic impact and elastic response for one free-drop wedge with stiffened panels. *Ocean Engineering*, 40: 1–14.
- Ma SY, Mahfuz H, 2012. Finite element simulation of composite ship structures with fluid structure interaction. *Ocean Engineering*, 52: 52–59.
- McVicar J, Lavroff J, Davis MR, Thomas G, 2018. Fluid–structure interaction simulation of slam-induced bending in large high-speed wave-piercing catamarans. *Journal of Fluids and Structures*, 82: 35–58.
- Mei TL, Zhang T, Maxim C, Evert L, Zou ZJ, 2020. Comparative study on ship motions in waves based on two time domain boundary element methods. *Engineering Analysis with Boundary Elements*, 111: 9–21.
- Nisham A, Terziev M, Tezdigan T, Beard T, Incecik A, 2021. Prediction of the aerodynamic behaviour of a full-scale naval ship in head waves using Detached Eddy Simulation. *Ocean Engineering*, 222, 108583.
- Ochi MK, Motter LE, 1973. Prediction of slamming characteristics and hull response for ship design. *Trans. SNAME*, 81: 144–190.
- Rajendran S, Fonseca N, Guedes Soares C, 2016. A numerical investigation of the flexible vertical response of an ultra large containership in high seas compared with experiments. *Ocean Engineering*, 122: 293–310.
- Rajendran S, Guedes Soares C, 2016. Numerical investigation of the vertical response of a containership in large amplitude waves. *Ocean Engineering*, 123: 440–451.
- Salvesen N, Tuck EO, Faltinsen OM, 1970. Ship motions and sea loads. *Trans. Soc. Nav. Archit. Mar. Eng. (SNAME)* 78: 1–30.
- Shi Y, Pan G, Yim SC, Yan GX, Zhang D, 2019. Numerical investigation of hydroelastic water-entry impact dynamics of AUVs. *Journal of Fluids and Structures*, 91, 102760.
- Shin H, Seo B, Cho SR, 2018. Experimental investigation of slamming impact acted on flat bottom bodies and cumulative damage, *International Journal of Naval Architecture and Ocean Engineering*, 10: 294–306.
- Singh SP, Sen D, 2007. A comparative study on 3D wave load and pressure computations for different level of modelling of nonlinearities. *Marine Structures*, 20: 1–24.
- Stavovy A, Chuang SL, 1976. Analytical determination of slamming pressures for high-speed vehicles in waves. *Journal of Ship Research*, 20: 190–198.
- Sun SL, Cheng Y, Cui J, Sun SY, 2020. Free fall water entry of a cone in three degrees of freedom. *Applied Ocean Research*, 101, 102273.
- Takami T, Matsui S, Oka M, Iijima K, 2018. A numerical simulation method for predicting global and local hydroelastic response of a ship based on CFD and FEA coupling. *Marine Structures*, 59: 368–386.
- Takami T, Iijima K, 2020. Numerical investigation into combined global and local

- hydroelastic response in a large container ship based on two-way coupled CFD and FEA. *Journal of Marine Science and Technology*, 25: 346–362.
- Terziev M, Tezdogan T, Incecik A, 2020. A posteriori error and uncertainty estimation in computational ship hydrodynamics. *Ocean Engineering*, 208, 107434.
- Tezdogan T, Incecik A, Turan O, 2016. Full-scale unsteady RANS simulations of vertical ship motions in shallow water. *Ocean Engineering*, 123: 131–145.
- Von Karman, 1929. The impact on seaplane floats during landing. NACA Technical Note No. 321.
- Wagner H, 1932. Über Stoss und Gleitvergange an der Oberfläche von Flüssigkeiten. *Zeitschrift für Angewandte Mathematik und Mechanik*, 12(4): 193–215. (in German)
- Watanabe I, Keno M, Sawada H, 1989. Effects of bow flare shape to the wave loads of a container ship. *Journal of the Society of Naval Architects of Japan*, 166: 259–266.
- Wang S, Guedes Soares C, 2013. Slam-induced loads on bow-flared sections with various roll angles. *Ocean Engineering*, 67: 45–57.
- Wang S, Guedes Soares C, 2016a. Stern slamming of a chemical tanker in irregular head waves. *Ocean Engineering*, 122: 322–332.
- Wang S, Guedes Soares C, 2016b. Experimental and numerical study of the slamming load on the bow of a chemical tanker in irregular waves. *Ocean Engineering*, 111: 369–383.
- Wang S, Guedes Soares C, 2017. Review of ship slamming loads and responses. *Journal of Marine Science and Application*, 16(4): 427–445.
- Wang JH, Wan DC, 2020. Application progress of computational fluid dynamic techniques for complex viscous flows in ship and ocean engineering. *Journal of Marine Science and Application*, 19(1): 1–16
- Wang Y, Wu W, Wang S, Guedes Soares C, 2020. Slam-induced loads of a three-dimensional bow with various pitch angles. *Journal of Offshore Mechanics and Arctic Engineering*, 142: 014502
- Wilson RV, Carrica PM, Stern F, 2006. Unsteady RANS method for ship motions with application to roll for a surface combatant. *Computers & Fluids*, 35(5): 501–524.
- Wu GX, Sun H, He YS, 2004. Numerical simulation and experimental study of water entry of a wedge in free fall motion. *Journal of Fluids and Structures*, 19: 277–289.
- Xie H, Liu F, Liu XY, Tang HY, 2020. Numerical prediction of asymmetrical ship slamming loads based on a hybrid two-step method. *Ocean Engineering*, 208, 107331.
- Xu GD, Duan WY, 2009. Review of prediction techniques on hydrodynamic impact of ships. *Journal of Marine Science and Application*, 8: 204–210.
- Yu PY, Li H, Ong MC, 2018. Numerical study on the water entry of curved wedges. *Ships and Offshore Structures*, 13(8): 885–898.
- Zhang L, Zhang JN, Shang YC, 2021. A practical direct URANS CFD approach for the speed loss and propulsion performance evaluation in short-crested irregular head waves. *Ocean Engineering*, 219, 108287.

This is a peer-reviewed, accepted author manuscript of the following research article: Jiao, J., Huang, S., Tezdogan, T., Terziev, M., & Guedes Soares, C. (Accepted/In press). Slamming and green water loads on a ship sailing in regular waves predicted by a coupled CFD–FEA approach. *Ocean Engineering*, 241, [110107]. <https://doi.org/10.1016/j.oceaneng.2021.110107>

Zhao R, Faltinsen OM, 1993. Water entry of two-dimensional bodies. *Journal of Fluid Mechanics*, 246: 593–612.